

3. $C\tau$ -FACTORY COLLIDER

3.1. Introduction

In the nineties of the past century, several projects of $c\tau$ -factories were discussed in the laboratories around the world that were engaged in the high energy physics investigations. All these facilities were planned to work with beam energy of 1÷3 GeV and a peak luminosity of about $10^{33} \text{ cm}^{-2} \text{ s}^{-1}$ [1, 2, 3, 4, 5, 6, 7, 8]. Different variants of monochromatization of the energy of particle collision were considered in order to study narrow resonances as well as the possibility of the production of transversely polarized particles (for precise energy calibration). The only project from the "family" of those $c\tau$ -factories which has been realized is now the BEPC II collider, commissioned at the laboratory IHEP (Beijing) in 2009 [9]. Its planned peak luminosity is $10^{33} \text{ cm}^{-2} \text{ s}^{-1}$.

The revival of the interest in these subjects and the beginning of work on the project of $c\tau$ -factory at BINP SB RAS is caused, first, by the outstanding results which were achieved at the B-factories at the laboratories of KEK (Japan) and SLAC (U.S.). These works culminated in the 2008 Nobel Prize in Physics to I. Nambu, M. Kobayashi and T. Maskawa. Though the high luminosity of the B-factories allowed obtaining some interesting results at low energies with the ISR method (proposed and developed at BINP), creation of a highly productive factory intended to study the physics of charmed particles and tau lepton is still a topical issue.

Second, the growing interest in the creation of the next-generation $c\tau$ -factory resulted from the discovery of a new and promising method of beam collision in an electron-positron collider, which allows raising the luminosity by two orders of magnitude at once as compared with the existing factories, without a significant increase in the beam intensity or the facility size or reduction in the bunch length. The idea was proposed by the Italian physicist Pantaleo Raimondi in 2006 when he studied the possibility of creating a high-luminosity B-factory [10]. Later the method was justified in joint works by P. Raimondi, M. Zobov (INFN/LNF, Frascati), and D. Shatilov (BINP, Novosibirsk) [18, 19] with simulation of the collision effects using the LIFE-TRAC software developed by Dmitry Shatilov. The new approach, described in detail below, was called "*Crab-Waist Collision with Large Piwinski Angle*". For brevity sake, we will refer to the new approach as the Crab Waist or CW collision method. Besides the $c\tau$ -factory in Novosibirsk, the CW collision method is used in the projects of the SuperB factory in Italy and the SuperKEKB factory (without the CW sextupoles at the moment) in Japan. In other words, all the projects of electron-positron circular super-colliders of the future are based on this new approach.

In 2008-2009, the new beam collision method was tried at the Φ -factory DAΦNE; the experiment results confirm the method to be promising and are in good agreement with the theory [13].

On the basis of the scientific tasks, which are discussed in detail in the section of the physics program of the $c\tau$ -factory, the following main requirements to the accelerator complex were stipulated:

- The beam collision energy in the center-of-mass system must vary from 2 GeV to 5 GeV, which allows experiments from the nucleon and antinucleon production energy to the region of the family of ψ -mesons and charmed baryons. Besides, such an energy range will allow using the results obtained on the VEPP-2000 and VEPP-4 colliders at BINP.
- The luminosity of the factory shall be not less than $10^{35} \text{ cm}^{-2} \text{ s}^{-1}$ in the high energy region and $\geq 10^{34}$ in the low energy one.
- The electron beam shall be polarized longitudinally at the interaction point (IP) [14, 15].
- Beams shall collide with equal energies; no asymmetry of the energies of the two beams is required.

- Since no schema for collision monochromatization without a significant decrease in the luminosity had been found, it was decided to abandon energy monochromatization, all the more so because the high luminosity allows effective exploration of the narrow resonance states without complicated monochromatization solutions.
- It was decided to abandon the need to have transversely polarized beams for precise calibration of energy. The energy will be measured by means of Compton back scattering of laser radiation on the particles of the circulating beam. This technique has been implemented recently on VEPP-4M [14] and shown a relative accuracy better than $\sim 10^{-4}$, which seems sufficient for the tasks of the new $c\tau$ -factory.

Among other requirements to the new project, the possibility of using, after modernization to increase the positron production, the BINP injection complex under commissioning is worth mentioning. To reduce the cost of the facility, its design implies using the existing BINP infrastructure, tunnels, buildings and premises. It was decided to create the systems, components and parts of the complex, relying on the technical and technological solutions available at BINP and widely adapting devices (electro- and superconducting magnets, the source of polarized electrons, elements of vacuum chamber and beam diagnostics, etc.) developed at BINP and supplied to other laboratories or working at the institute.

3.2. Crab waist collision method

When two flat beams collide, a small vertical beta function β_y at the IP is one of the major conditions for high luminosity. However, due to the divergence of the beam, β_y is limited by the longitudinal size of the particle bunch σ_z (so-called *hour-glass* effect), which can not be made very small because of the growth of the collective effects. The electron bunch length achieved by now for characteristic beam currents of $1\div 2$ A is $\sim 6\div 10$ mm, which limits the minimum vertical beta function at the IP and consequently the luminosity of the traditional electron-positron colliders.

This problem can be solved with the recently proposed Crab Waist scheme for collision of two bunches, which can significantly (up to two orders of magnitude) increase the luminosity of e^+e^- colliders without reducing the bunch length or increasing its intensity [10]. The new approach involves two basic ideas.

The first idea is to arrange a collision of two beams at an angle in the horizontal plane θ so that the so-called Piwinski parameter

$$\phi = \frac{\sigma_z}{\sigma_x} \tan \frac{\theta}{2} \approx \frac{\sigma_z}{\sigma_x} \frac{\theta}{2} \quad (3.1)$$

be large enough, where σ_z is the bunch length and σ_x is its rms size in the transverse direction. The schematic of such a collision is shown in Fig. 3.1.

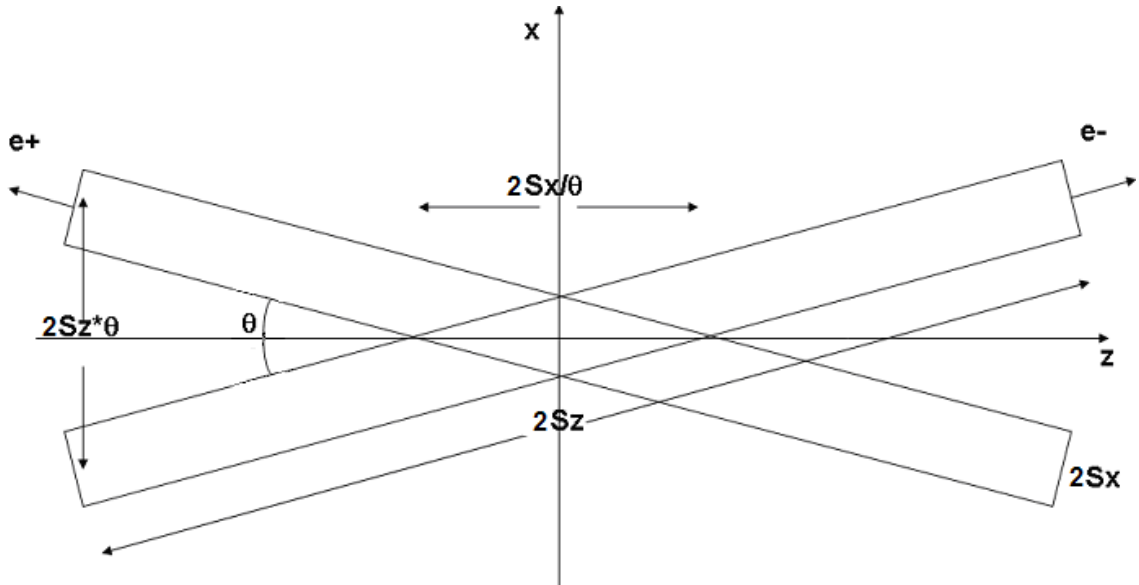


Fig.3.1 Beam collision with a large Piwinski parameter

One can see from Fig. 3.1 that now the vertical betatron function is limited not by the bunch length σ_z but by the size of the beam interaction region: $\beta_y \approx \sigma_x / 2\theta$; and if the transverse beam size σ_x is small, the vertical betatron function can also be made very small.

In the general case, the luminosity and the parameters of the space charge can be written as [12]

$$L \propto \frac{N \xi_y}{\beta_y}, \quad \xi_y \propto \frac{N \beta_y}{\sigma_x \sigma_y \sqrt{1 + \phi^2}} \quad \text{и} \quad \xi_x \propto \frac{N}{\varepsilon_x (1 + \phi^2)}. \quad (3.2)$$

From these formulas we can see that at $\phi=0$ we cannot increase the luminosity through reducing the vertical beta function (the *hour-glass* limitations) or increasing the number of particles per bunch N (restrictions on the collision parameter $\xi_y \sim 0.1$). If $\phi \gg 1$, first, the region of beam interaction (and thus β_y) may become very small (fractions of millimeter), and the reduction in the beam size is compensated with a large ϕ so that the ξ_y value remains in the required limits. Moreover, the horizontal parameter of the space charge ξ_x , decreases as ϕ^1 , which is also a positive factor.

Note that luminosity expression (3.2) looks the same as for a head-on collision of beams, and the dependence on the intersection angle enters only the parameters of the space charge. Fig. 3.2 depicts beam collision at a small Piwinski angle and a large one.

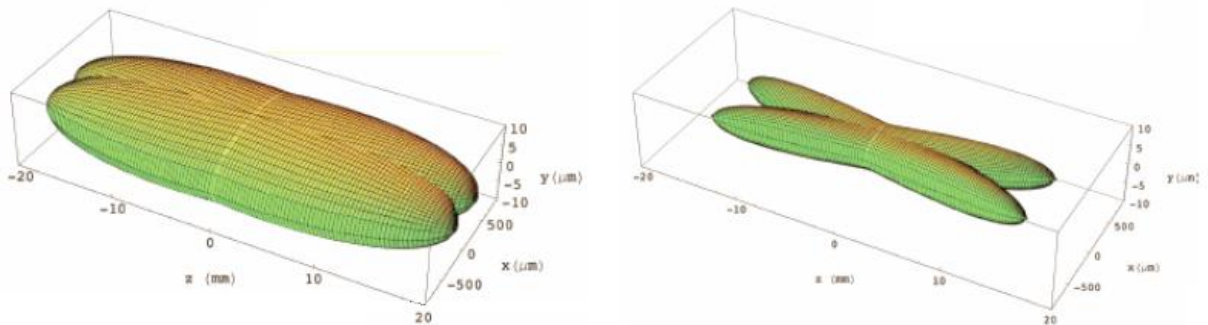


Fig. 3.2 Beams colliding with a small (left) and large Piwinski parameter. For the sake of clarity the transverse scale was increased much as compared with the longitudinal one.

At a CW collision, the increase in the Piwinski parameter occurs due to the increase in the angle of intersection and the reduction in the transverse beam size. Therefore, it is clear that for this approach, unlike the traditional facilities for colliding beams, the horizontal emittance must be small, which allows applying the well-developed methods of designing low-emittance synchrotron radiation sources.

Let us estimate the characteristics of a collider with energy $E = 2$ GeV and a circumference of about 800 m, which is determined by the convenience of the setup accommodation in the BINP area. Let the beam intersect at the angle $2\theta = 60$ mrad, then a luminosity of 10^{35} $\text{cm}^{-2}\text{s}^{-1}$ requires parameters as listed in Table 3.1

Table 3.1 Beam parameters

Beam current, I	A	1.7
Number of particles in the beam, N		2.7×10^{13}
Number of bunches, n_B		390
Bunch current, I_b	mA	4.4
Bunch length, σ_z	mm	10
Emittance, $\varepsilon_x/\varepsilon_y$	nm-rad	8 / 0.04
β at the IP, β_x^*/β_y^*	mm	40/0.8
Beam size at the IP, σ_x/σ_y	μm	17.9/0.179
Piwinski parameter, Φ		15.1
Space charge parameter, ζ_x/ζ_y		0.0044/0.13
Luminosity, L	$\text{cm}^{-2}\text{s}^{-1}$	1.0×10^{35}

It should be mentioned that none of the parameters listed in the table limits (in the technical sense) the creation of the facility. Such (and even higher) currents were obtained at the B-factories (KEK and SLAC) and the F-factory (Frascati); such emittances have long been common for the modern synchrotron radiation sources, and a bunch length of $\sim 6 \div 10$ mm has been achieved at both colliding beam facilities and SR sources.

Various authors have long considered the problem of beam collision at an angle and shown (e.g. [17, 18]) that in such a scheme modulation of the vertical motion by horizontal betatron oscillations leads to a large (as compared with a frontal collision) number of coupled resonances which impede the realization of the above advantages. To solve this problem and correct the betatron coupling, the Crab Waist transformation of beam at the IP (Fig. 3.3) was suggested.

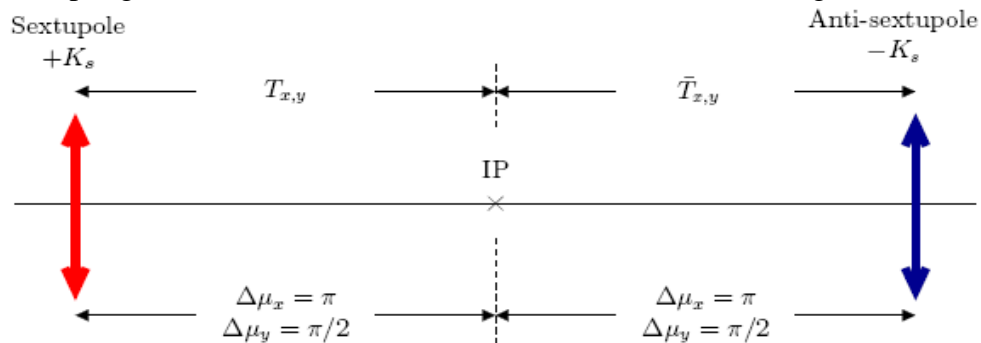


Fig. 3.3 Schematic arrangement of the CW sextupole magnets

For this purpose, two sextupole magnets are placed from two sides of the IP. The transformation of the vertical coordinate and the pulse through the first (along the beam) "thin" sextupole magnet with the integrated strength (ml)

$$y = y_0, \quad y' = y'_0 + (ml) \cdot x_0 y_0$$

can be formally considered as vertical focusing of the beam with the focal length depending on the horizontal coordinate:

$$y' = y'_0 + K(x_0) \cdot l \cdot y_0, \quad \text{где} \quad K(x_0) = m \cdot x_0.$$

Then the position of the minimum of the vertical betatron function varies depending on the horizontal coordinate of the particle. In other words, the minimum of the vertical betatron function (waist) rotates as in Fig.3.4.

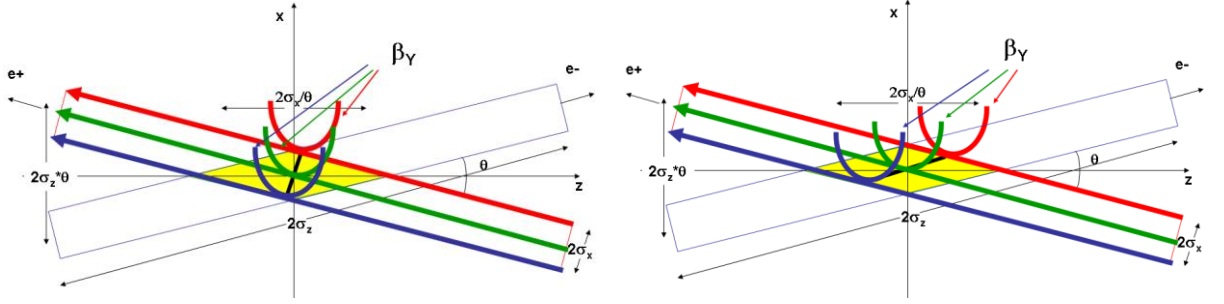


Fig. 3.4. Position of the minimum of the vertical betatron function before (left) and after (right) the CW transformation.

At a certain betatron phase advance between the CW sextupoles and the IP ($\Delta\mu_x = n \cdot \pi$, $\Delta\mu_y = (2m+1) \cdot \pi/2$, where n and m are integers) and a certain integral strength of the lens

$$(m \cdot l) = \frac{1}{2\theta} \frac{1}{\beta_y^* \beta_y} \sqrt{\frac{\beta_x^*}{\beta_x}}, \quad (3.3)$$

where β^* and β denote the beta-function at the IP and in the azimuth of the “crab” sextupole, correspondingly, the minimum of the vertical betatron function rotates so that the dependence of the vertical betatron phase at the IP on the horizontal coordinate of the test particle gets suppressed, which efficiently kills both the betatron coupling resonances and their synchrobetatron satellites.

Fig.3.5 shows a luminosity scan in dependence on the position of the nonperturbed betatron tune for the case when the “crab” transformation is off (right) or on (left). One can see that in the latter case many coupling resonances are killed and the “good” luminosity region is much bigger.

The Crab Waist concept of collision was experimentally verified at the Φ -factory DAΦNE in Italy [13]. Through relatively small modifications, the beams were made to collide at a large Piwinski angle, and sextupole magnets were placed around the IP to provide the CW map. However, it was impossible to obtain a small vertical betatron function, because of the insufficient flexibility of the ring lattice. Nevertheless, the suppression of the collision effects due to the “crabbing” of the vertical beta waist alone increased the luminosity ~ 3 times as compared with the best results of the previous collider configuration (the green dots in Fig. 3.6 should be compared with the yellow and red ones). Turning the “crab” sextupoles off (the blue dots in the graph in Fig. 3.6) decreased the luminosity and made it impossible to work with large currents, because of the collision effects. The experiment clearly demonstrated the validity and potential of the Crab Waist collision concept.

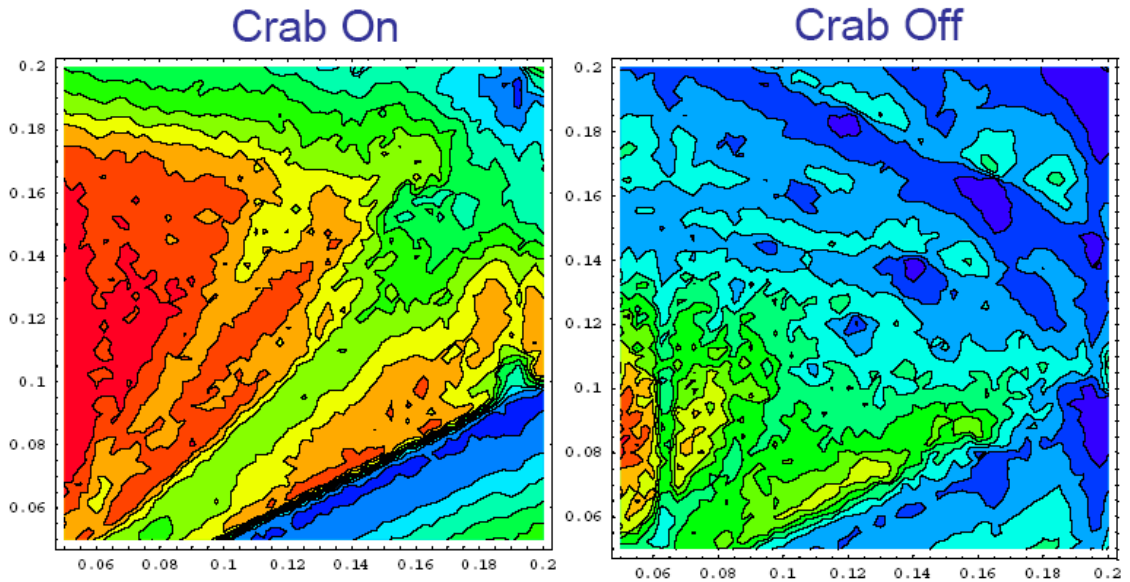


Fig. 3.5 Luminosity as a function of the working point of the betatron tunes (the horizontal and vertical axes correspond to the tune fractional part part). The red and blue colors show large and small luminosity.

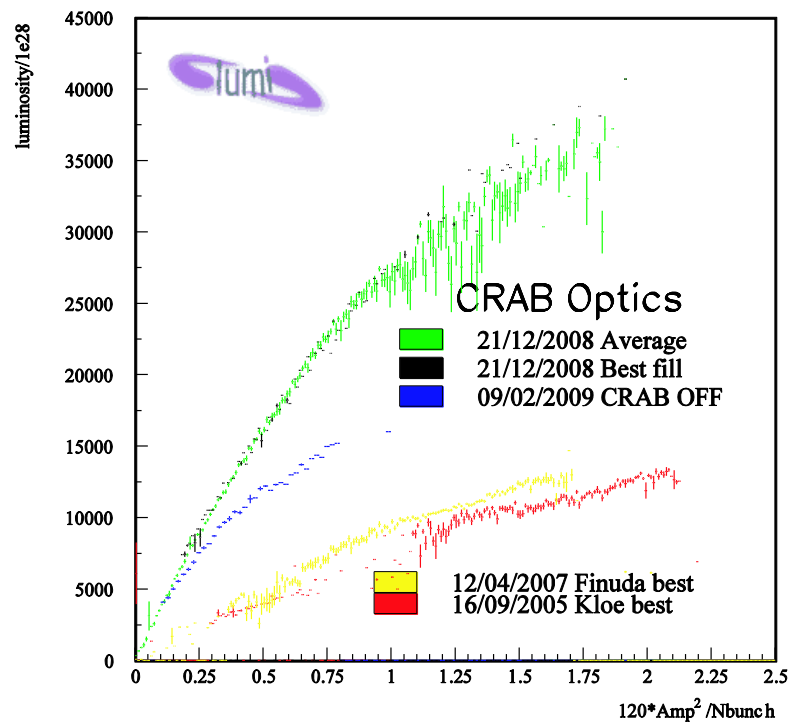


Fig. 3.6 Measured DAΦNE luminosity in peak in dependence on the colliding beam intensity. The red and yellow points indicate the best results in the previous configuration (without CW optics); the green and blue points are for the CW sextupoles on and off, correspondingly.

3.3. Collider parameters definition

There is one collision point in the collider, where, depending on the experimental program, one or two disposable detectors can be placed:

(1) An universal detector will operate throughout the energy range. The main luminosity integral will be gained at fixed points of 1.5 GeV (J/ψ -meson) to 2.5 GeV (charmed baryons) in the beam. At every such point, the collider collects statistics during a long time, and the luminosity must be maximum possible. The largest integral is estimated to be gained at the $\psi(3770)$ point. Besides that, a few scannings over energy from 1 GeV to 2.5 GeV will be carried out.

(2) A detector with a dense polarized target. The high luminosity at the nucleon production threshold and the longitudinal polarization of electron beam make the $c\tau$ -factory the only possible source of polarized antinucleons. The experiment consists in the examination of the spin-dependent characteristics in the process of annihilation of nucleons and antinucleons. For this, the polarized target should to be placed as close to the place of particle production as possible. Unlike the universal detector, this architecture looks more compact and simple, including the simplification of the superconducting winding that forms the longitudinal field in the detector, which can be used to increase the luminosity at the expense of another final doublet with large aperture and another angle of beam collision.

So, the efficiency of the facility operation should be optimized for energies of 1.5 GeV to 2.5 GeV, the maximum efficiency (as to the luminosity, life time, operation time, etc.) reached at energy of 1.88 GeV, where a suppressing luminosity integral gain is predicted. This task is solved subject to the following considerations:

- High single-bunch luminosity, which is reached due to the application of the Crab Waist conception and the sub-millimeter vertical beta-function at the IP.
- The multi-bunch mode, which implies the application of the two-ring scheme.
- A high bunch charge at a small length (~ 10 mm).
- Efficient control of the damping parameters (emittance, damping time, etc.) to provide high luminosity over the entire energy range.
- The final focus that ensures obtaining an ultimately small beta-function at the beam IP; placement of the “crab” sextupoles; correction of the high chromaticity of the lenses of the final focus; etc.
- Provision of high-level longitudinal polarization of electron beam over the entire energy range.
- Continuous injection at the experimental energy with the positron current intensity providing achievement of high luminosity.

Luminosity. High luminosity in the single-bunch mode is achieved due to the Crab Waist scheme. The beam collision at a large Piwinski angle makes the interaction region significantly smaller than that at a frontal collision, when this region is equal to the length of the bunch. Thus, with no fear of the *hour-glass* effect, we can reduce the vertical beta function at the IP. Another positive moment also worth noting is that there is no problem of parasitic IPs in the scheme with a large Piwinski angle as the beams are moved several transverse dimensions apart already at the distance of the bunch length.

The ultimate value of the collision parameter ξ_y when the CW technology is applied is 2 to 3 times higher than at a head-on collision of beams. This is achieved due to the two “crab” sextupoles placed near the IP so that they do not perturb motion over the entire ring and rotate the vertical size at the IP in dependence on the transversal coordinate. Thus, the phase modulation induced by the beam-beam effects is suppressed as well as the betatron and synchrobetatron coupling resonances.

The maximum ξ_y value depends on the time of betatron oscillation damping in the storage ring, τ_x . Analysis of the parameters of electron-positron colliders shows that the ξ_y parameter is inversely proportional to the cube root of the damping time. Simulation of the beam-beam (BB)

effects suggests that for $\zeta_y \approx 0.15$ the damping time should be ~ 30 ms. To maintain a high ζ_y value throughout the energy range it is necessary to keep the damping time constant.

On the one hand, when the energy decreases, the luminosity will decrease proportionally to the energy itself. On the other hand, the influence of the BB effects will increase, which is expressed as the dependence of the ζ_y parameter on the energy. Exceeding the maximum ζ_y value leads to a decrease in the lifetime of the beam. Accordingly, to maintain a high luminosity it is necessary to compensate the energy change with other values entering ζ_y . The angle of beam intersection as well as the horizontal and vertical beta functions at the IP depends on the design of the final focus. So, it would be better to keep these values constant as the energy varies. It is proposed to optimize the luminosity via changing the bunch length: when the energy decreases, the bunch length increases, the maximum ζ_y value remains constant, while the luminosity decreases linearly. Increasing the bunch length is useful for reducing the role of collective effects and intra-bunch scattering.

The final focus design. Compact superconducting two-aperture magnets are planned to be used as the final doublet of quadrupole lenses. The distance from the IP to the cut of the yoke of the first (defocusing) quad is 60 cm and the gradient is 10.7 kG/cm. The application of two-aperture magnets allows passing beams along the magnet axis, reducing the unwanted background load of the detector from the synchrotron radiation. An additional complication of the final focus system is associated with the need to compensate the longitudinal field of the detector, which leads to the transversal rotation of the beams and introduces the betatron coupling.

Damping time and beam emittance. The phase-space volume and the damping time should remain constant throughout the energy range.

$$\alpha_x = \tau_x^{-1} = C_\alpha E^3 \frac{I_2}{\Pi}, \quad (3.4)$$

where $C_\alpha = 2113.1 \text{ m}^2/\text{GeV}^3/\text{s}$, Π is the storage ring circumference, I_2 is the second radiation integral (it is taken that the dimensionless damping decrement $J_x = 1$), which includes the contribution from the magnetic structure of the ring, I_{20} , and the wigglers, i_2 :

$$I_2 = I_{20} + i_2, \quad i_2 = \frac{1}{2} h_w^2 L_w, \quad (3.5)$$

where $h_w = B_w/BR$, B_w is the maximum field in the wiggler, BR is the magnetic rigidity, $L_w = \lambda_w N_w$ is the total length of the wiggler, λ_w is the field period, N_w is the number of periods. In order to keep the damping time constant throughout the energy range, there are superconducting wigglers mounted in the magnetic structure of the storage ring, which allows efficiently tuning the integral I_2 .

Note that the energy loss by radiation per turn is unambiguously associated with the damping time:

$$U_0 = C_\alpha \gamma^2 \frac{\Pi}{\tau_x}.$$

A decrease in the damping time will lead to an increase in the power of the energy loss by radiation, which should be compensated by the accelerating RF system:

$$P = U_0 I,$$

where I is the total beam current.

Besides, the superconductive snakes allow monitoring the horizontal phase-space volume (I_{50} and i_5 denote the contribution from the storage ring and the snakes, correspondingly):

$$\varepsilon_x = C_q \frac{\gamma^2}{J_x} \frac{I_5}{I_2}, \quad I_5 = I_{50} + i_5, \quad i_5 = \frac{1}{15\pi^3} h_w^5 \lambda_w^2 L_w \left(\bar{\beta}_x + \frac{20\pi^2 \eta_0^2}{\bar{\beta}_x h_w^2 \lambda_w^2} \right), \quad (3.6)$$

where $\bar{\beta}_x$ is the horizontal beta function value averaged over the snake length; η_0 is the dispersion function at the center of the snake. The last expressions have been obtained for the sinusoidal model of snake. It is desirable to install the superconducting snakes in places with low beta function in order to minimize their influence on the beam.

Number of particles and bunch length. The maximum number of particles per bunch is determined by the *fast head-tail instability*. The threshold current of this effect is proportional to the bunch length and should be taken into account when choosing the latter. A large bunch charge distorts the potential well of the accelerating RF field and increases the bunch length. In addition, the microwave instability may lead to increase in the energy spread of the beam as well as in the bunch length. This effect has a threshold nature and it is efficient to work at beam current values below the threshold. Nevertheless, it is necessary to have a reserve in the accelerating voltage because the only way to overcome the bunch stretching due to the current is to reduce the bunch length at the zero current. The beam current and bunch length values for the $c\tau$ -factory are selected basing on the experience with the values already achieved at the present B-factories.

The number of bunches. The number of bunches (total current) depends on the power of the high-cost accelerating RF system. The number of bunches determines the system for suppression of multi-bunch instabilities. Suppressing the multi-turn ion instability in the electron ring requires a 5-10% gap in the bunch repetition. Fast ion instability may lead to increase in the vertical dimension of bunches at the end of the train. A vertical size increase can also occur in the positron ring as a result of the interaction with the electron clouds that are formed from the secondary particles near the beam axis. The point of the instability is proportional to the beam current and inversely proportional to the inter-bunch distance.

Loss of particles. Two effects leading to loss of particles dominate at the $c\tau$ -factory: the intrabeam scattering (Touschek effect) and the single bremsstrahlung, the latter being almost independent of the particle energy and determined by the single-bunch luminosity, which will fall with decreasing energy. Correspondingly, the loss due to the single bremsstrahlung will also fall. On the other hand, the Touschek loss will increase with decreasing beam energy. However, this dependence is not very strong, because the total phase-space volume increases with decreasing energy: the transverse emittance is preserved and the beam length increases.

Injection. To ensure a high integrated luminosity it is necessary to maintain an appropriate average current, for which the "continuous" injection mode is suggested. The choice of the injection frequency is determined by the efficiency of data recording (the ratio between the detector dead time and the background loading). The maximum frequency is determined by the repetition rate of the positron injection complex and equals 50 Hz. To reduce the dead time of the detector we suggest simultaneous injection of electrons and positrons, which requires their simultaneous acceleration in the linear accelerator with a shift of $\lambda/2$. Such a method has been implemented at KEKB.

Polarization. The longitudinal polarization of electron beam at the IP is one of the key issues of the $c\tau$ -factory. For this purpose a source of polarized electrons is allowed for in the design, at the exit from which one can get any spin direction and thus with all future rotations at the point of injection, the beam will have a correct spin direction. Two alternatives for obtaining the longitudinal polarization at the IP of the base ring were considered: (1) a scheme with polarization recovery, and (2) a scheme using the "Siberian snakes". In the first case, two spin rotators are used,

which are located near the IP and perform spin rotation in a small region, the spin motion staying unperturbed over the rest of the ring. In this case, the spin rotators occupy a relatively small space and the integral of the longitudinal field is small, which is a positive moment in terms of the betatron coupling. A significant drawback of this scheme is the presence of (three) spin resonances in the working energy range, one of which falls on the point of τ -lepton production, and the other, on the Λ -baryon region. That is why the second scheme was chosen. However, to obtain a high degree of polarization throughout the energy range, there must be five or more Siberian snakes. To reduce the spin-orbit coupling the Siberian snakes must alternate with superconducting damping snakes. In this regard, the parameters under which the design luminosity is calculated are chosen for a relatively large (by modern standards) betatron coupling of 0.5%.

General arrangement of the setup. Subject to the above, the $c\tau$ -factory consists of the following facilities

- Injector of positrons
- Polarized electrons injector
- Full-energy linear pre-accelerator
- Double-ring collider

Two independent (electron and positron) injectors can effectively produce particles without losing time for changing the polarity of the magnets and implement a scheme of simultaneous acceleration of two bunches. The linear accelerator (unlike the synchrotron) allows accelerating the polarized particles without losing the degree of polarization as well as accelerating large charges of particles with smaller loss and higher frequency.

The main ring of the $c\tau$ -factory is a racetrack storage ring consisting of arcs, the technical straight section for injection and the experimental section (shown schematically in Fig. 3.7).

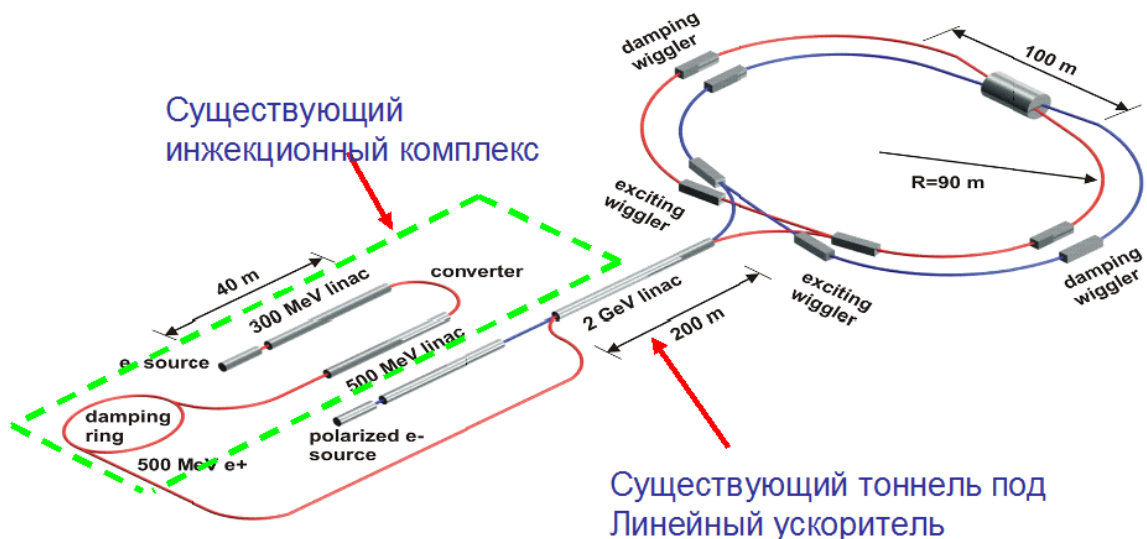


Fig. 3.7 Schematic of the complex

The arcs comprise four Siberian snakes alternating with four superconducting wigglers. The parameters of the arcs were chosen so as to obtain the required dimensions and the radiation parameters of the beam. The dipole magnet is selected subject to the requirement to the damping time. The optics of the periodicity elements must ensure the expected beam emittance. At 2.5 GeV the damping time should be 30 ms and the beam emittance should be 8 nm·rad with the

wigglers turned off. The technical straight section accommodates the accelerating RF system, the fifth Siberian snake, and the injection equipment. In the midpoint of the technical straight section a vertical separation of the beams is arranged.

The experimental straight section is intended to focus the beams at the IP. The first quadrupole doublet is placed inside the detector. The lenses are to be superconducting and placed in one cryostat. The next lens system is designed to match the optical functions of the final doublet with the rest of the structure and correct the chromatic and geometric aberrations. The experimental straight section also comprises a system of collimators to reduce the halo of lost particles and improve the background situation for the detector. Since the energy loss per turn is rather large, it would be reasonable to place the energy calibration system near the IP, in one of the drifts.

The main parameters of the collider are presented in Table 3.2

Table 3.2 Main parameters of the *ctau*-factory

Energy	1.0	1.5	2.0	2.5	GeV
Circumference, Π	766.6				M
Revolution frequency, f_0	391.06				kHz
Revolution time, τ_0	2.557				μs
Orbit compaction factor, α	8.949	9.053	9.078	9.087	$\times 10^{-4}$
Wiggler field, B_w	49.23	36.80	25.07	0	Kg
Accelerating voltage, V_{RF}	310	900	990	1000	kV
Energy loss per turn, U_0	170	256	343	434	keV
Damping time, $\tau_x / \tau_z / \tau_s$	30/30/15				ms
Coupling factor, k	0.5				%
Horizontal emittance, ε_x	8				nm·rad
Vertical emittance, ε_y	40				$\pi\text{m}\cdot\text{rad}$
Energy spread, σ_E	1.009	9.953	8.435	7.378	$\times 10^{-4}$
Bunch length, σ_z	1.6	1.06	1	1	cm
Particles per bunch, N_0	$7 \cdot 10^{10}$				
Bunch current, I_0	4.4				mA
Number of bunches, N_b	390				
Total number of particles, N	$2.73 \cdot 10^{13}$				
Total current, I	1.7				A
Beta functions at the IP, β_x / β_y	4/0.08				cm
Beam size at the IP, σ_x / σ_y	17.9/0.18				μm
Intersection angle, 2θ	60				mrad
Piwinski angle, φ	26.91	18.50	16.82	16.82	
Hour-glass effect	0.906	0.906	0.906	0.906	
Collision parameter, ξ_y	0.15	0.15	0.12	0.095	
Single-bunch luminosity, L_0	1.61	2.43	2.57	2.57	$\times 10^{32} \text{ cm}^{-2} \text{ s}^{-1}$
Светимость, Luminosity L	0.63	0.95	1.00	1.00	$\times 10^{35} \text{ cm}^{-2} \text{ s}^{-1}$

3.4. Magnetic lattice

3.4.1. General description of the collider

The magnetic lattice of the $c\tau$ -factory is designed subject to the following main points:

- Provision of small beam emittance throughout the energy range ($\varepsilon_x = 8 \text{ nm}\cdot\text{rad}$, $\varepsilon_y = 0.04 \text{ nm}\cdot\text{rad}$).

- Ensuring high productivity of the collider at $E = 1.0 - 2.5$ GeV
- Optimization of the setup parameters is carried out in the region of the largest luminosity integral $E \approx 1.9$ GeV; the maximum luminosity at this energy must be 10^{35} cm⁻²s⁻¹ or more.
- The magnetic lattice shall allow placing the “crab” sextupoles in the azimuth with the required betatron phase advance.
- Ensuring high-degree longitudinal polarization of electron beam at the IP over the whole energy range.

To realize these conditions it is proposed to create the collider on the basis of two rings separated in the radial direction and having one main IP in the experimental section and a "parasitic" IP in the straight technical section (Fig. 3.8). The beams intersect in the radial direction in the technical section and are moved apart in the vertical direction by magnets that create a local orbit bump. This scheme of the rings allows accumulating sequences of large numbers of bunches and providing a total intersection angle of 60 mrad, which is required for the CW collision. For a luminosity of 10^{35} cm⁻² s⁻¹ the ring should accommodate 390 bunches with a total current of 1.7 A and a 10% gap in this sequence to prevent accumulation of ions in the electron beam potential. The facility perimeter required to accommodate the given number of bunches is about 767 m.

To obtain acceptable polarization throughout the energy range of the electron beam it is necessary to place five polarization insertions with superconducting solenoids in the ring with a bending angle between the devices of about 72°.

The implementation of the CW scheme with an angle of beam intersection at the main IP of 60 mrad imposes requirements on the beam emittance ($\varepsilon_x = 8$ nm-rad, $\varepsilon_y = 0.04$ nm-rad), which should not change throughout the energy range. Simulating the BB effects shows that $\nu_x = 0.54$ and $\nu_y = 0.57$ is the optimal choice for the operating point of the betatron tunes. The required damping time of transverse oscillations should not exceed 30 ms, and that of the longitudinal oscillations, 15 ms. To control the emittance and provide the necessary radiation damping, two inserts with superconducting damping wigglers are placed in each arcs of the collider. The systems of magnets and quadrupoles adjacent to the segment of the damping wigglers excite a dispersion function to correct the beam emittance.

The rings of the collider also contain matching sections to adjust the periodicity cells of the half-rings with the experimental section and the technical straight. The technical straight comprises the segment for moving the colliding beams apart.

A schematic view of the collider of the $c\tau$ -factory is shown in Fig. 3.8. The collider lattice consists of two identical storage rings of the same circumference, which are spaced from each other in the horizontal plane. The rings are symmetrical with respect to the axis passing through the main and parasitic IPs. We can distinguish several functional sections in the electron and positron storage rings, denoted in Fig. 3.8 with the following numbers:

1. The IP, the detector and the superconducting lenses of the final focus that ensures the desired focusing of the beams at the IP. The building for assembling, maintaining and placing the detector systems is located over this site. The IP is in immediate adjacency to the two long (70 m) collision segments, where the chromaticity correction sections and the "crab" sextupole lenses are located.
2. The technical section is intended to accommodate the injection system, the accelerating cavities and the beam separation drift. The building which will house the power supply system of the magnets, the RF generators, the control equipment, the power supplies for the vacuum pumps, the control room and other premises necessary for the functioning of the complex is planned to be built over the technical gap.
3. The big and small half-rings, consisting of the same elements but slightly differing in the length of the periodicity cell.

4. The spin rotators located uniformly over the angle of beam rotation in every $\approx 72^\circ$ and creating a longitudinally polarized electron beam at the IP with polarization sufficient for the experiments.
5. Four sections of the damping wigglers that ensure the required radiation parameters and control the emittance.
6. Four sections for matching the periodicity cells of the small and large half-rings with the experimental and technical sections; these sections also include the sections for zeroing the dispersion function.

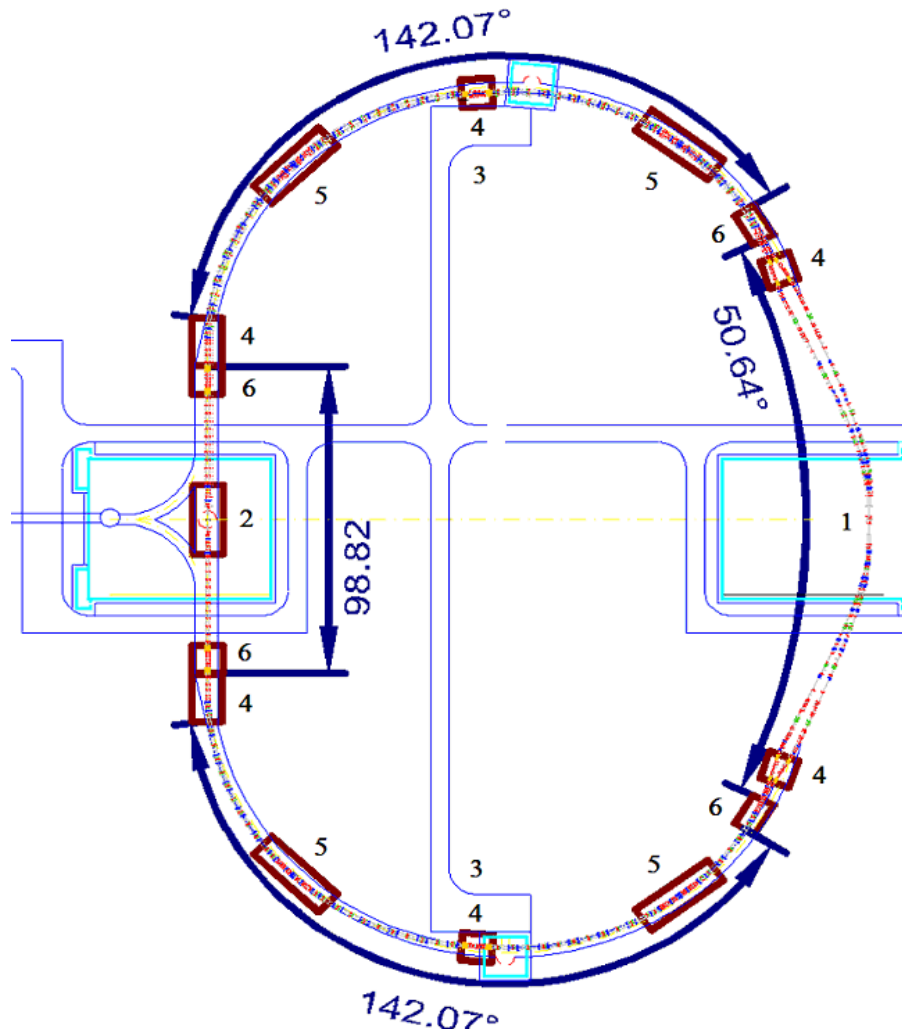


Fig. 3.8 Scheme of the collider of the τ -factory. See the designations and explanations of the main components of the complex in the text.

3.4.2. Interaction region

The interaction region (IR) shall

- ensure low beta function values at the IP,
- provide small geometrical aberrations,
- have a length and an orbit bend angle that agree with the infrastructure (tunnel) being designed,
- ensure local correction of the chromaticity.

Main parameters used to optimize the interaction region (IR) are given in Table 3.3.

Table 3.3 Main parameters of the collision segment of the C-tau-factory

Energy, GeV	2
Particles per bunch	$7 \cdot 10^{10}$
Number of bunches	390
Beam current, A	1.7
β_x , mm	40
β_y , mm	0.8
ε_x , nm rad	8
Coupling factor, $\varepsilon_y/\varepsilon_x$, %	0.5
Bunch length, σ_s , mm	9
Total intersection angle, mrad	60
Collision parameter, ξ_y	0.12
Geometrical luminosity, $\text{cm}^{-2}\text{s}^{-1}$	$1.1 \cdot 10^{35}$
Luminosity subject to the bunch length, $\text{cm}^{-2}\text{s}^{-1}$	$1.0 \cdot 10^{35}$
Piwinski angle, φ , rad	15

Obtaining small beta function values at the IP requires placing the final lenses as close to the IP as possible. The solenoids that compensate the longitudinal field of the detector are situated before the lenses. Since the winding of the main solenoid of the detector envelopes the final lens doublet, the lenses are enclosed in a shield solenoid, in order to use uncoupled optics in the lenses.

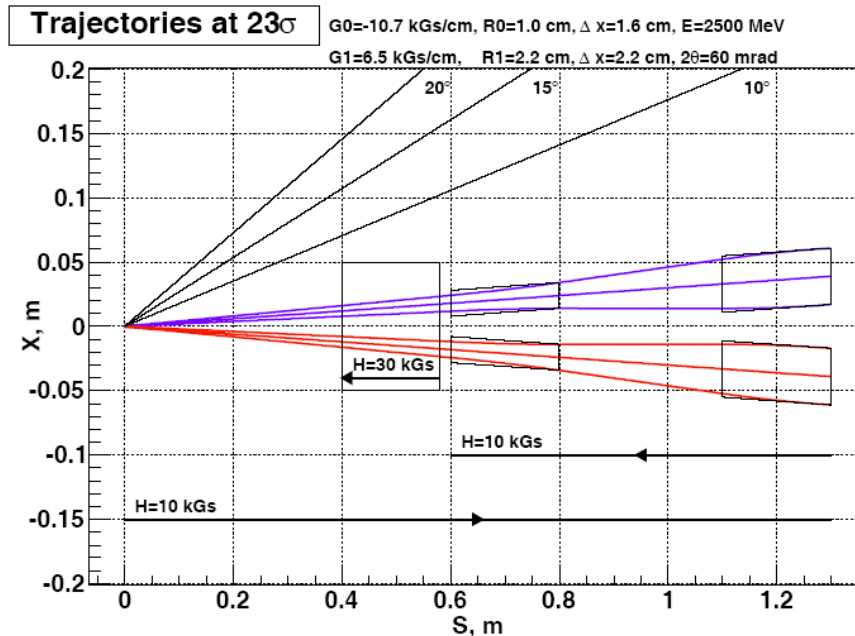


Fig. 3.9 Scheme of the collision region. The beam trajectories and envelopes, the compensating, shield and main solenoids and the 10°, 15° and 20° cones are shown.

The scheme in Fig.3.9 shows the location of the main elements in the collision region and the beam trajectories. The distance from the IP to the edge of the nearest lens is 60 cm; the place for the compensating solenoid less than 20 cm long is 40 cm away from the IP. The final focus lenses are 20 cm long. One lens is located 30 cm away from the other. This distance was

optimized in view of obtaining the maximum acceptance and minimizing the beta functions in the lens. The final lens is made with two apertures for the incoming and outgoing beams to pass through the center of their apertures and avoid subjecting to the dipole field, which generates synchrotron radiation and creates a substantial background load on the detector. The chosen intersection angle allows creating a two-aperture lens and getting the required luminosity.

Small beta function values at the IP lead to large values in the final lenses, so non-interleaved pairs of sextupoles separated by the $-I$ transformation within each pair are used to compensate the chromaticity. To facilitate the compensation of the chromatic effects, the optics of the collision segment is based on telescopic transformations for the main parts of the collision segment [19].

The optical functions of the collision segment are shown in Fig. 3.10.

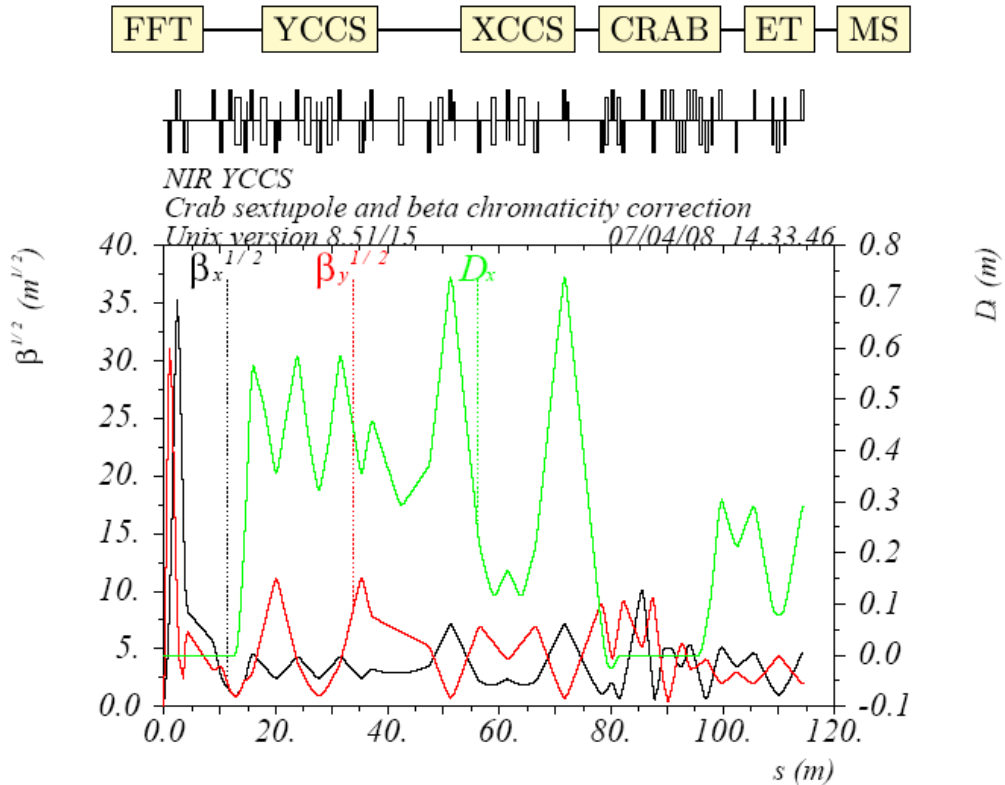


Fig. 3.10 Lattice functions of the collision segment. Top: the schematic diagram of the segment: FFT is the final telescope, YCCS and XCCS are the chromaticity correction sections, CRAB is the section of the “crab” sextupoles, ET is the section for zeroing the horizontal dispersion function, MS is the section for matching the IR with the arcs.

The first (final) telescope consists of two doublets of quadrupole lenses. The telescope parameters have been chosen to meet the following conditions: the beta functions at the exit shall be matched with the chromaticity correction sections; if the beta function chromaticity equals zero at the IP, it must be maximal at the exit from the final telescope.

Further goes the chromaticity correction section, which adjusts the horizontal and vertical chromaticity of the collision region. It begins with a dipole to excite dispersion for the chromatic sextupoles and a doublet of lenses to provide the required phase advance and beta functions. The chromaticity of the beta functions is mainly excited by the doublet of the final lenses. There should be sextupoles with a difference of $n\pi$ in the corresponding betatron phase to correct this chromaticity. It is location of the second sextupoles that corrects the second-order geometric aberrations, so a minus identity transformation is observed within the pair. The third-order geometric aberrations that arise due to the finite length of the sextupoles are compensated by the correction sextupoles with a strength of about 10% of that of the main sextupole, which are placed (at a small distance) after each main sextupole. The section ends with four lenses and one dipole, thus

providing zero dispersion and telescopic transformation. Further goes the section of the crab sextupole intended to provide the phase advance required to install the crab sextupole and the beta function values required for the sextupole strength to be reasonable and to minimize the nonlinear dispersion and the chromaticity of the beta functions in the place of the crab sextupole. This section ends with four lenses providing the telescopic transformation from the IP to the end of the collision segment.

The strengths of the main sextupoles are chosen allowing for the condition of chromatic transparency of the whole IR. That is, if there are zero chromaticities of the beta and alpha functions of nonlinear dispersion at the entrance to the section, at the exit they must be zero too. In this case, the main sextupoles are not enough, so one more sextupole (not breaking the $-I$ pair) is installed, with a strength less than 30% of that of the main sextupoles. To reduce the strength of these additional sextupoles, the section for horizontal chromaticity correction is shifted in phase relative to the corresponding final lens [20]. The IR is asymmetric with respect to the IP. Because of the angle between the beams the orbits diverge, which is adjusted via matching the sections between the collision segment and the half-rings of the $c\tau$ -factory.

3.4.3. Magnetic lattice of the storage ring

The optical functions of the collider are shown in Fig.3.11. Since the beta functions are small at the point of beam collision, the betatron functions reach values of about kilometer (and more) in the final focus lenses.

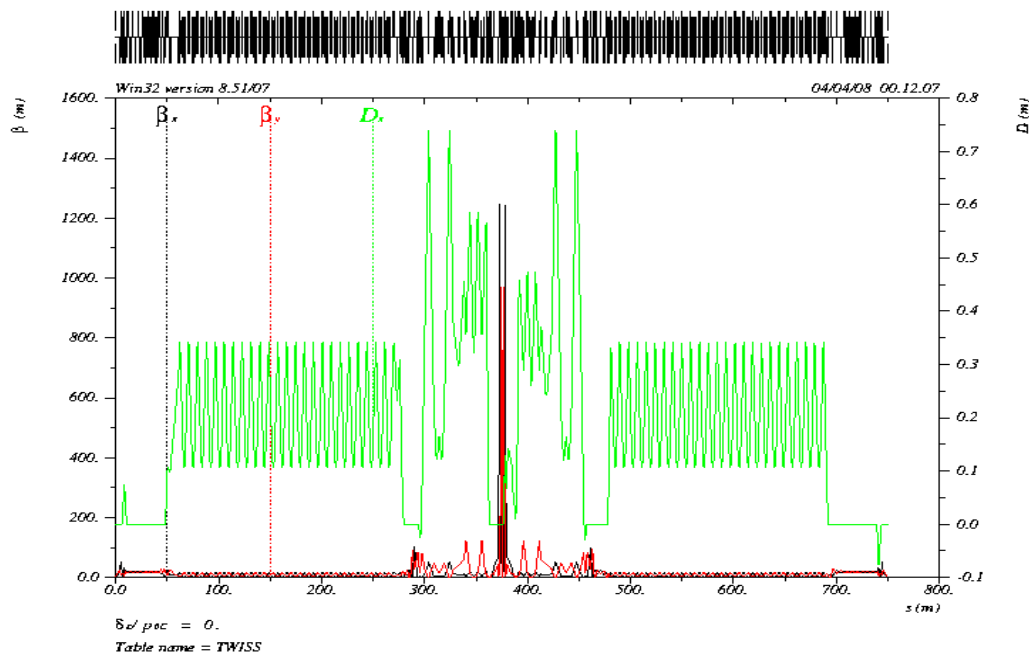


Fig. 3.11 Optical functions of the $c\tau$ -factory.

As a result, the final focus quadrupoles are a strong source of chromaticity (both of the betatron tunes and of the optical functions), the high chromaticity orders playing a significant role. Thus the influence of the field errors and the nonlinearities, including the edge ones, of the lenses of the final focus increases as well as the requirements to the manufacturing accuracy of such lenses.

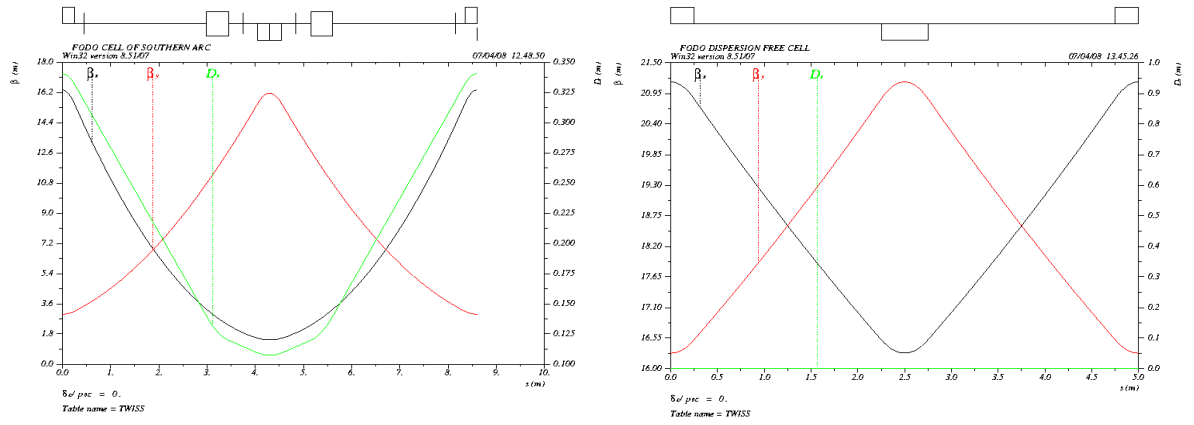


Fig. 3.12 Periodicity cells of the arcs and the technical straight section.

Fig. 3.13 shows the cells for matching the straight (experimental and technical) sections with the arcs. These regions are intended to match the betatron functions of the sections and the arcs and make the dispersion function zero in the sections.

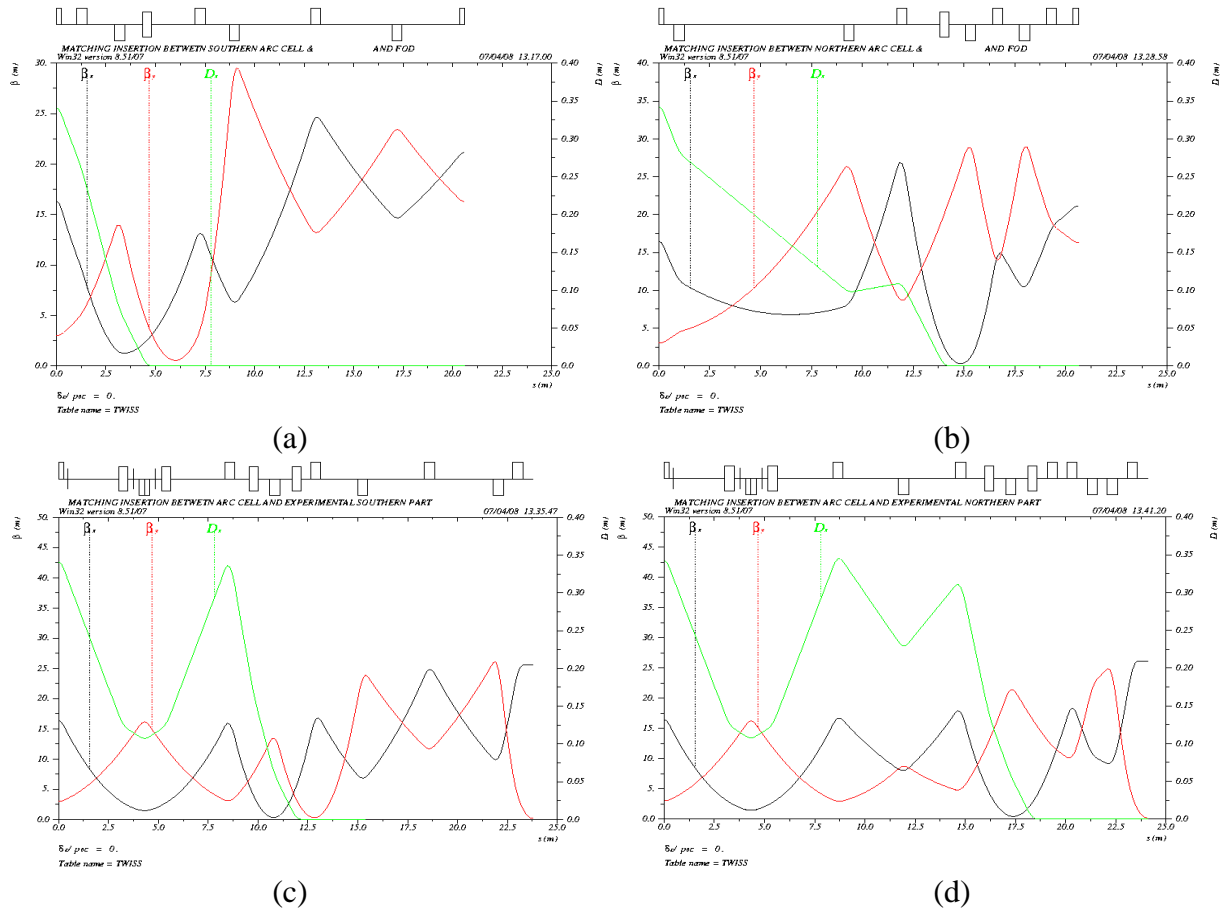


Fig. 3.13 Matching regions for the technical, (a) and (b), and experimental, (c) and (d), sections. The left and right rows show the matching with the small and large arcs, correspondingly.

The optical functions of the collision region are shown in Fig. 3.10. It is also necessary to note the presence of large (several hundred meters) beta functions in the chromaticity correction sections, which requires careful attention to the quality of the field of the magnetic elements.

The two arcs of each (electron and positron) storage ring are slightly different in size, for arrangement of the beam intersection. However, the periodicity cells of the small and large half-rings, which are intended to solve the problem of obtaining a small emittance, hardly differ from each other in the behavior of the optical functions, which are shown in Fig. 3.12. The cell is a

modified FODO lattice in which the short bending magnets are shifted to the defocusing lens (shown at the center of the cell in Fig. 3.12). Such a cell is still compact, but it allows a fairly low emittance due to the fact that both the horizontal beta function and the dispersion function in the magnet are close to the minimum. The periodicity cell of the technical gap, also shown in Fig. 3.12, is a simple FODO structure; the dispersion function is made zero here by a special matching segment (see below).

The magnetic structure of the storage ring includes 128 dipole magnets, 216 quadrupole and 204 sextupole lenses, 16 wigglers to control the polarization and 12 wigglers to control the damping parameters.

3.4.4. Controlling the emittance and the damping parameters

To obtain the maximum luminosity of the $c\tau$ -factory in the required energy range it is necessary to effectively control the radiation damping parameters of the accelerator in order to maintain a constant horizontal emittance ($\varepsilon_x = 8$ nm-rad) (nm-rad) and the damping time ($\tau_{x,y} \approx 30$ ms, $\tau_z \approx 15$ ms). Superconducting wigglers are planned to be installed for this purpose on both rings. The wigglers parameters can be estimated from the following considerations.

The dependence of the damping time on the energy and the wigglers parameters has the following form (3.4):

$$\tau_{x,y,s} = \frac{const_{x,y,s}}{E^3(I_{20} + i_2)}, \quad (3.7)$$

where I_{20} and i_2 are the second radiation integral from the accelerator lattice and the wigglers, correspondingly. Varying i_2 with energy as

$$i_2(E) = I_{20} \left(\frac{E_0^3}{E^3} - 1 \right), \quad (3.8)$$

where $I_2(E_0) = I_{20} = 0.79 \text{ m}^{-1}$ for $E_0 = 2.5 \text{ GeV}$, it is possible to make the damping time (3.7) a constant function of the energy.

It follows from (3.8) that the maximum value of the damping integral the wigglers shall ensure for the minimum energy $E = 1.0 \text{ GeV}$ must be $i_2(E) = 11.5 \text{ m}^{-1}$. The second radiation integral from the wiggler field is written as

$$i_2 = \frac{L_w}{\rho_w^2} \text{ for a piece-wise approximation of the poles, and}$$

$$i_2 = \frac{L_w}{2\rho_w^2} \text{ for a sinusoidal model of the wiggler field, where } L_w \text{ is the total length of all}$$

the wiggler and ρ_w is the particle turning radius for the maximum field of the wiggler. It can be seen that the piecewise-constant approximation gives, for the same length and amplitude of the wiggler field, a twofold win in i_2 . For such an approximation to be valid, the wiggler field period should exceed the pole gap by far. On the other hand, the longer the period, the greater the deviation of the beam orbit from the axis, and thus the requirements for the value of the horizontal aperture of the snake and the quality of the field tighten. Basing on the experience of fabrication of superconducting wigglers by BINP, a reasonable compromise is a wiggler with a pole gap of ≈ 40 mm and a period length of ≈ 200 mm. In this case, it is quite possible to use a piecewise constant model of the field.

Choosing (subject to the free space available) $L_w = 6.4$ m, we obtain the maximum field of the snakes $B_{w\max} = 4.5$ T at $E = 1.0$ GeV, which seems quite acceptable for the chosen parameters of the wiggler.

To ensure the constancy of the damping time of the betatron and synchrotron oscillations throughout the beam energy range, the wiggler field amplitude should depend on the energy as follows:

$$B_w(E) = B\rho(E) \cdot \sqrt{\frac{I_{20}}{L_w} \left(\frac{E_0^3}{E^3} - 1 \right)}, \quad (3.9)$$

where $B\rho(E)$ is the rigidity of the magnetic system. The dependence of the wiggler field on the energy at our parameters is shown in Fig. 3.14.

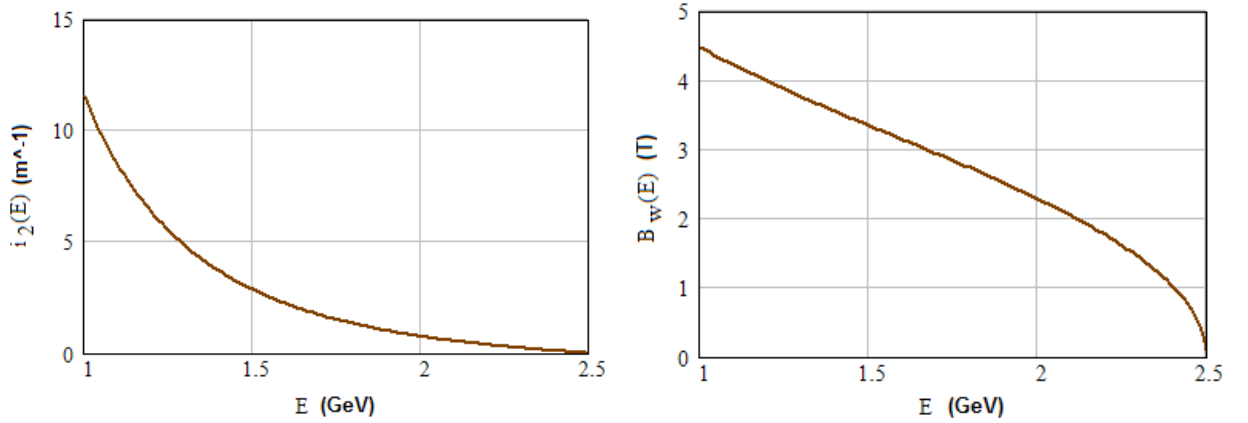


Fig. 3.14 Dependence of the radiation integral (left) and the wiggler field amplitude on the beam energy.

The dependence of the emittance on the energy and the wiggler parameters is written as

$$\varepsilon_x(E) = \text{const} \cdot E^2 \frac{I_{50} + i_5}{I_{20} + i_2}. \quad (3.10)$$

Requiring the emittance to be constant at energy and substituting (3.8) into (3.10), we have

$$i_5(E) = I_{50} \left(\frac{E_0^5}{E^5} - 1 \right), \quad (3.11)$$

where $I_5(E_0) = I_{50} = 6.8 \cdot 10^{-4} \text{ m}^{-1}$ for $E_0 = 2.5$ GeV, which together with the second radiation integral I_{20} ensures the horizontal emittance $\varepsilon_x = 8$ nm-rad at the maximum energy and the wiggler field off.

It follows from (3.11) that at $E = 1.0$ GeV the wiggler shall produce the integral $i_5(E) = 6.6 \cdot 10^{-2} \text{ m}^{-1}$. For a sinusoidal model, the fifth radiation integral can be written as

$$i_5 = \frac{8}{15\pi} \frac{i_2}{\rho_w} \cdot \left(5 \frac{\eta_0^2}{\beta_x} + \bar{\beta}_x \theta_w^2 \right), \quad (3.12)$$

where $\bar{\beta}_x$ is the horizontal beta function averaged over the wiggler length, η_0 is the «residual» dispersion function in the wiggler straight section, and the maximum angle of the beam orbit deviation in the wiggler field is computed as

$$\theta_w = \frac{\lambda_w}{2\pi\rho_w}. \quad (3.13)$$

To ensure the emittance constancy throughout the energy range, we have to equate (3.12) to (3.11) over this range. Since the condition of keeping of the damping time constant unambiguously determines the behavior of $i_2(E)$, $\rho_w(E)$ and $\theta_w(E)$, the only thing we can change in (3.12) is the structure function $\bar{\beta}_x$ or η_0 . It is advantageous to fix a rather small $\bar{\beta}_x \approx 0.5 \div 1$ m in order to reduce the influence of the wiggler field on the beam dynamics. In this case, one can obtain the constancy of the emittance (together with that of the damping time) if the dispersion function of the wiggler segment depends on the energy as follows:

$$\eta_0^2(E) = \frac{3\pi}{8} \bar{\beta}_x \frac{I_{50}}{I_{20}} \frac{\rho_w(E)}{E^2} \frac{E_0^5 - E^5}{E_0^3 - E^3}. \quad (3.14)$$

This expression takes into account that the second term in the brackets is much less than the first one:

$$\eta_{0\min} \gg \frac{1}{\sqrt{5}} \bar{\beta}_x \theta_w$$

Here $\eta_{0\min} \approx 50$ mm corresponds to energy of 1 GeV, while $\bar{\beta}_x \theta_w / \sqrt{5} \approx 10$ m at the same energy.

In the region of high energies, $E \approx E_0$, there is practically no need in the wigglers because the magnetic structure of the storage ring ensures the required emittance and damping. In the region of small energies, $E < E_0$, estimate expression (3.12) can be written as

$$\eta_0^2(E) \approx \frac{3\pi}{8} \bar{\beta}_x \frac{I_{50}}{I_{20}} \rho_w(E) \frac{E_0^2}{E^2},$$

taking into account that $\rho_w(E) \sim E$, $\eta_0 \sim 1/\sqrt{E}$.

Fig. 3.15 shows the dependence of the dispersion function on the energy in the wiggler segment, calculated in accordance with (3.14). The minimum dispersion value is $\eta_{0\min} \approx 50$ mm at energy of 1 GeV, and then it grows up to ~ 150 mm at energy of 2.5 GeV.

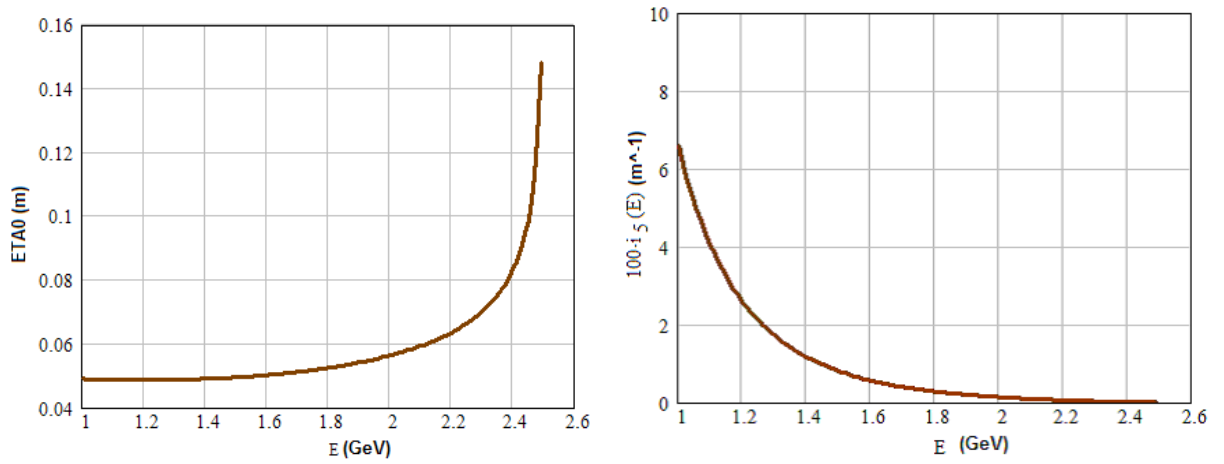


Fig. 3.15 “Residual” dispersion function in the wiggler segment (left) and the fifth radiation integral produced by the wiggler to preserve the emittance over the operation energy range of the $c\tau$ -factory.

For the above-chosen wiggler parameters, the maximum angle of deviation and the orbit drift in dependence on the energy are shown in Fig. 3.16.

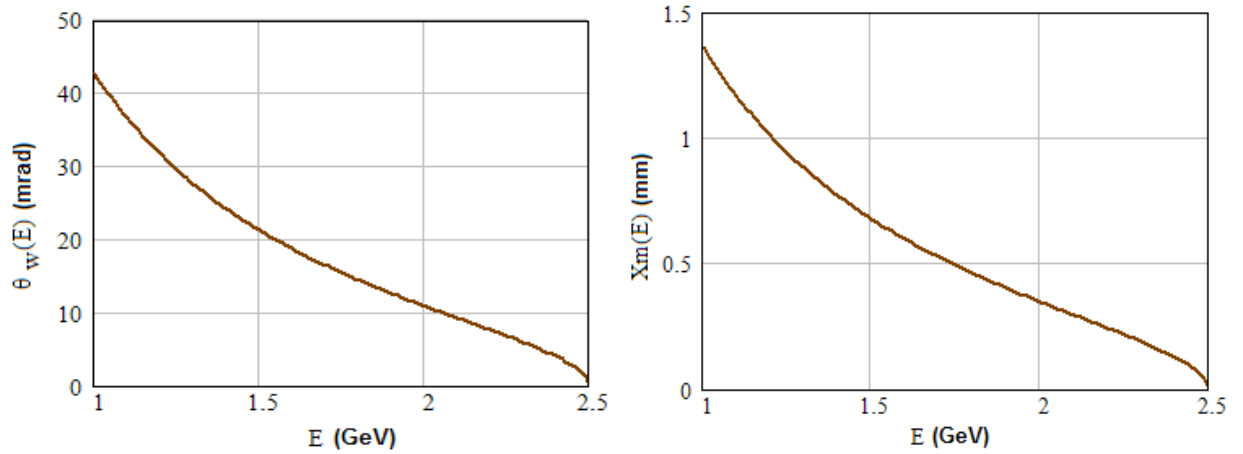


Fig. 3.16 Maximum angle of deviation (left) and orbit drift in the wiggler field.

Since in real life a (small) change in the dispersion function in the “wiggler” segment will inevitably be accompanied by a change (also small) in the average horizontal beta function entering (3.12), the maximum luminosity should be set “in accordance with the effect”.

3.4.5. Correction of chromaticity and the dynamical aperture

For the $c\tau$ -factory, the study and optimization of the dynamical aperture have a number of features that are more or less identical for all projects of colliders with the Crab Waist collision scheme.

Small values of the betatron functions (especially of the vertical one) at the IP result in large chromaticity values (of the tunes and the optical functions) generated by the final focus section:

$$\xi^* \approx -l / \beta^*,$$

where l is the distance from the IP to the quadrupole lens, and β^* is the corresponding betatron function at the IP. For $\beta_y^* < 1$ mm, the typical vertical chromaticity is $\xi_y^* \sim -10^3 \dots -10^4$. The horizontal chromaticity is smaller but it may also be as high as a few hundreds.

This chromaticity is corrected locally by the sextupole magnets located, if possible, close to the final focus lenses. The strengths of the sextupoles are large and the dynamical aperture turns out to be small. To avoid this, we place the magnets in pairs as in Fig.3.17.

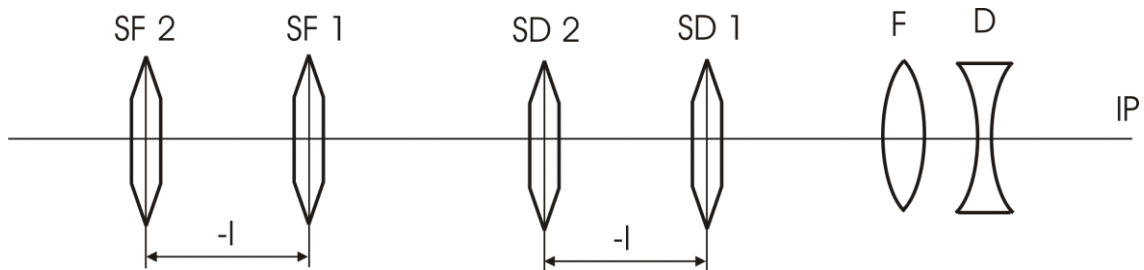


Fig. 3.17 The beam IP, the doublet of the quadrupole lenses of the final focus (FD), and the two pairs of the sextupole magnets to correct the vertical (SD) and horizontal (SF) chromaticity.

If the matrix of the optical transformation between the sextupole magnets of the pair is equal to minus unity, such a system does not generate higher-order aberrations outside the pair and therefore does not affect the dynamic aperture [19].

However, this principle is true only for a model with infinitely thin (zero-length) sextupole lenses. Allowing for the finite length leads to the fact that only the quadratic aberrations are fully compensated, but the higher ones still stay, and in view of the large values of the betatron functions severely limit the dynamic aperture [20] as shown in Fig. 3.18.

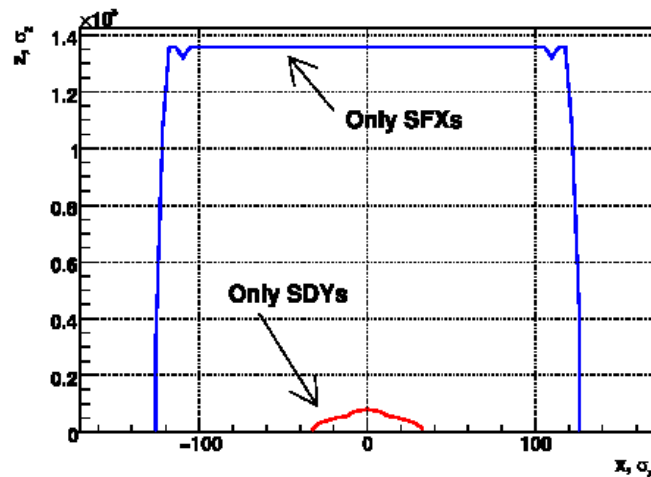


Fig. 3.18 Restriction of the dynamical aperture with pairs of sextupole lenses compensating the chromaticity of the collision region subject to their nonzero length.

A method to correct this effect was proposed in [20]. The method consists in adding a pair of corrective sextupole lenses also located in phase with the $-l$ transformation to the pair of the main chromatic sextupole lenses (Fig. 3.19). Strength of the corrective lenses of 3-10% of the basic lenses turns out to be enough to significantly (several times) increase the dynamic aperture (Fig. 3.20).

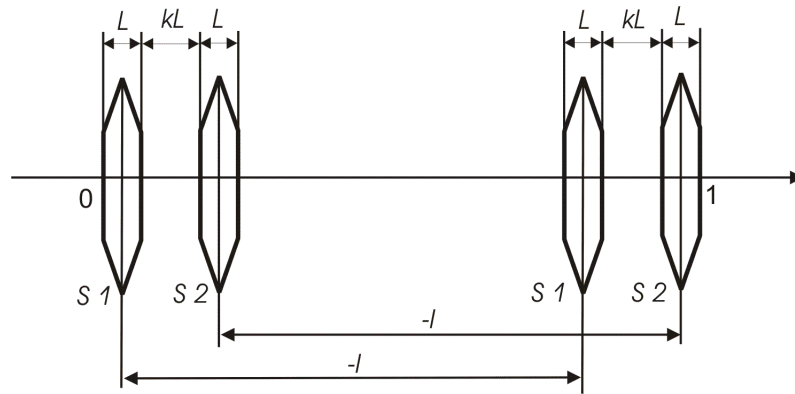


Fig. 3.19 Addition of the corrective pair of sextupole lenses (S2) to the main ones (S1).

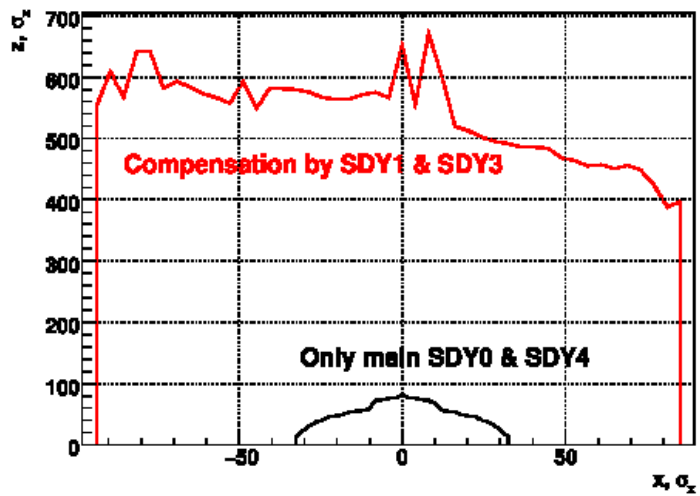


Fig. 3.20 Increasing the dynamical aperture with the corrective sextupole lenses.

Since the condition of placing a pair of a "crab" sextupole lenses is essentially identical to a pair of chromaticity-correction lenses placed through the $-l$ transformation and the strengths of the "crab" lenses are great, the same effect – reduction in the dynamic aperture if the non-zero length of the magnets is taken into account – is observed here too (Fig. 3.21, left).

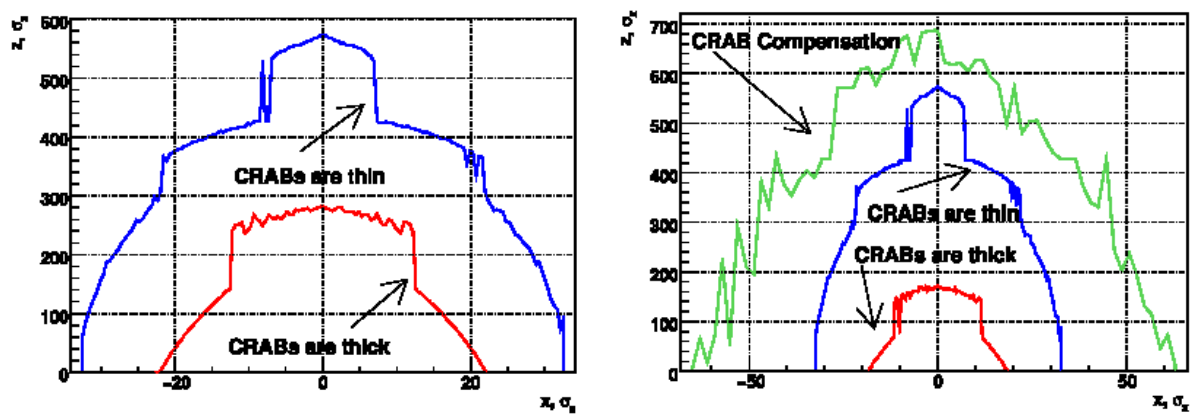


Fig. 3.21 Reducing the dynamic aperture with the "thick" "crab" sextupoles (left) and correction of the effect with an additional pair of lenses (right).

Placing an extra pair of compensating lenses of small strength can also essentially increase the resulting aperture here (Fig. 3.21, right).

In addition to the effect already considered, which is fundamental for the CW-colliders, it is necessary also to ponder the following sources of nonlinear perturbation:

- The boundary fields of the final focus quadrupole lenses and the chromaticity-correction cells (since the betatron functions here reach the extreme values of a few hundred meters).
- The sextupole lenses correcting the chromaticity in the periodicity cells of the half-rings. This problem is similar to that which occurs in the modern synchrotron radiation sources with low emittance.
- The extreme smallness of the vertical betatron function at the IP can lead to significant kinematic effects, which also must be considered.

3.4.6. Final focus lenses

Fig.3.22 schematically shows the vacuum chamber of the final focus section. The vacuum chamber parameters determine the design of the final focus elements and other magnetic elements which are located here. The beryllium vacuum chamber of a vertex detector 300 mm long from one side (the total length of the chamber is 600 mm) begins from the IP. The following 100 mm are reserved for the detector electronics. In this region the inner diameter and the thickness of the vacuum chamber are 40 mm and 1 mm, correspondingly. The angle between the beams is 60 mrad here. Then goes a transition gap approximately 150 mm long, where the chamber bifurcates into two chambers, each 20 mm in diameter (Figure 3.23). This gap houses a superconducting (SC) solenoid compensating the detector field, the solenoid aperture repeating the vacuum chamber aperture.

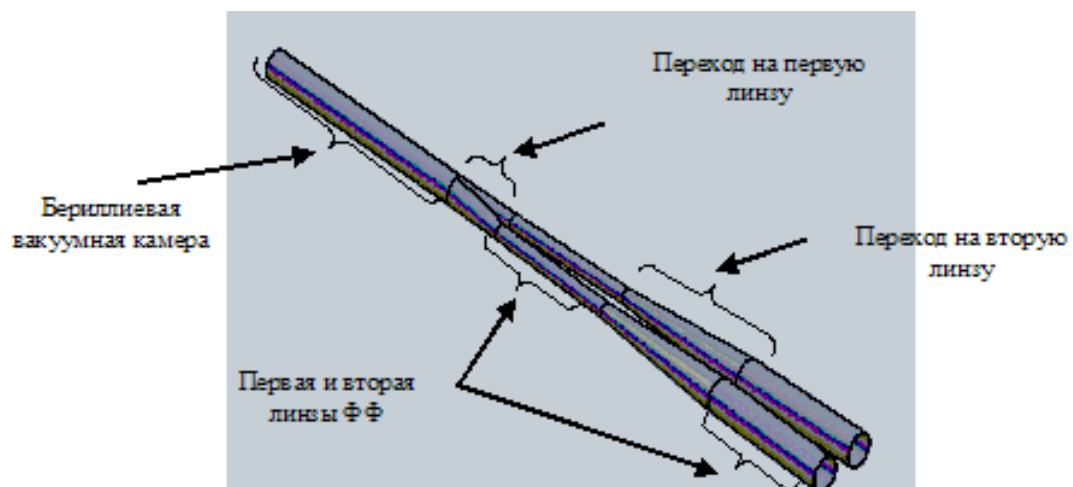


Fig. 3.22 Vacuum chamber of the IP (schematic).

Further is the superconducting solenoid which ensures the absence of longitudinal field in the FF lens. The solenoid consists of two parts with different apertures (SSH1 and SSH2). The aperture of the solenoids is determined by the overall size of the lens and the vacuum chamber at the end of the solenoid. The first lens begins inside the shielding solenoid and is almost completely shielded from the longitudinal field of the compensating solenoid and the detector field. The first FF lens as well as the second one is 200 mm long. There is 300 mm of empty area between them. The first shielding solenoid covers the entire lens plus at least 50-100 mm of the empty area. This place requires careful and accurate elaboration since it determines the solid angle of the detector. The second shielding solenoid begins around the middle of the empty space between the FF lenses; the length of the solenoid is determined by the design of the yoke of the detector and also requires a detailed study.

The parameters of the magnetic elements of the FF section are presented in Table 3.4.

Table 3.4 Parameters of the FF lenses and solenoids at energy of 2.5 GeV

Name	L_{eff} (mm)	s (mm)	B_{max} (kG), G_{max} (kG/)	R_{ap} , mm	$\Delta B/B$, $\Delta G/G$ (%)	Type
L_0	0.595	0	10	40	1	IP
$SC0$	100	45	-45	45	1	SC compact solenoid
$SSH1$	350-600	55	-10	-	1	SC shielding solenoid
$SEQ0$ ($NEQ0$)	200	60	-10.7	10	0.01-0.05	2-aperture SC quadrupole lens
$SSH2$	700-900	85	-10	-	1	SC shielding solenoid
$SEQ1$ ($NEQ1$)	200	110	6.5	22	0.01-0.05	2-aperture SC quadrupole lens

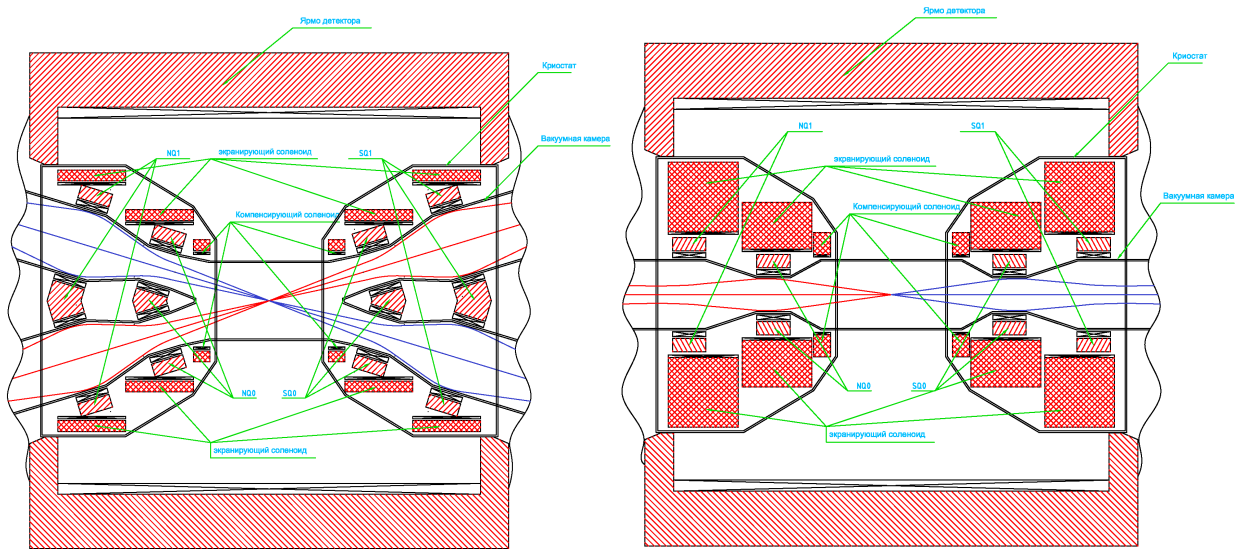


Fig. 3.23 Top view (left) and the side view (right).

One of the most important elements in the final focus section are the first (defocusing) and second (focusing) quadrupole lenses that provide beam focusing at the IP.

The yoke of the first lens $SEQ0$ ($NEQ0$) is located at a distance of 600 mm from the IP (the distance is indicated along the trajectory). The effective length of the lens is 200 mm; the overall length with the coils is less than 300 mm. The general view of the lens is shown in Fig. 3.24. Calculations of the magnetic field (two-dimensional model) show that the accuracy of the gradient $\Delta G/G_0 \leq 4 \cdot 10^{-4}$ is achieved over the whole range of energy (Table 3.5, Fig. 3.25) in the working aperture of the lens $R = 10$ mm. The field expansion harmonics listed in Table 3.5 have the following form:

$$B(x) = \sum_n A_n \cdot x^{n-1}.$$

The calculations also show that the dependence of the gradient on the energy is, with good accuracy, linear, despite the fact that the magnetic field induction in the yoke of the lens reaches 21-23 kG. The yoke of the lens is made of vanadium permendure with the magnetization curve shown in Fig. 3.26.

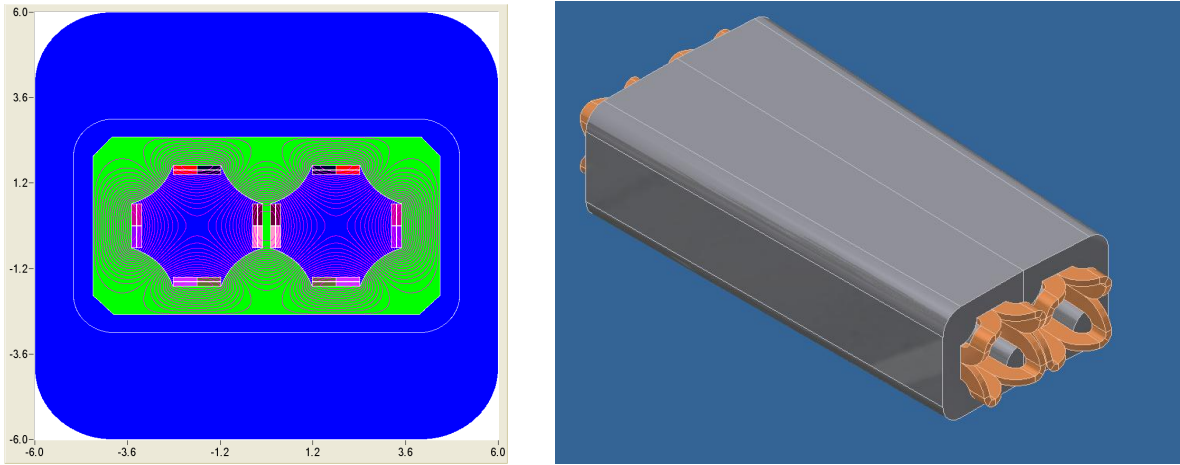


Fig. 3.24 FF lens *SEQ0* (*NEQ0*). The cross section and the flux paths (left) and the general view (right).

Table 3.5. Main harmonics of the lens *SEQ0* (*NEQ0*)

	2.5 GeV	2 GeV	1.2 GeV
n	$A_n, (\text{kG}/\text{cm}^{n-1})$	$A_n, (\text{kG}/\text{cm}^{n-1})$	$A_n, (\text{kg}/\text{cm}^{n-1})$
2	-10.97	-9.08	-5.32
6	-0.0038	-0.0031	-0.0019
10	0.0021	0.0018	0.0011
14	0.0006	0.00046	0.00027
18	-2.2E-05	-1.8E-05	-1.1E-05

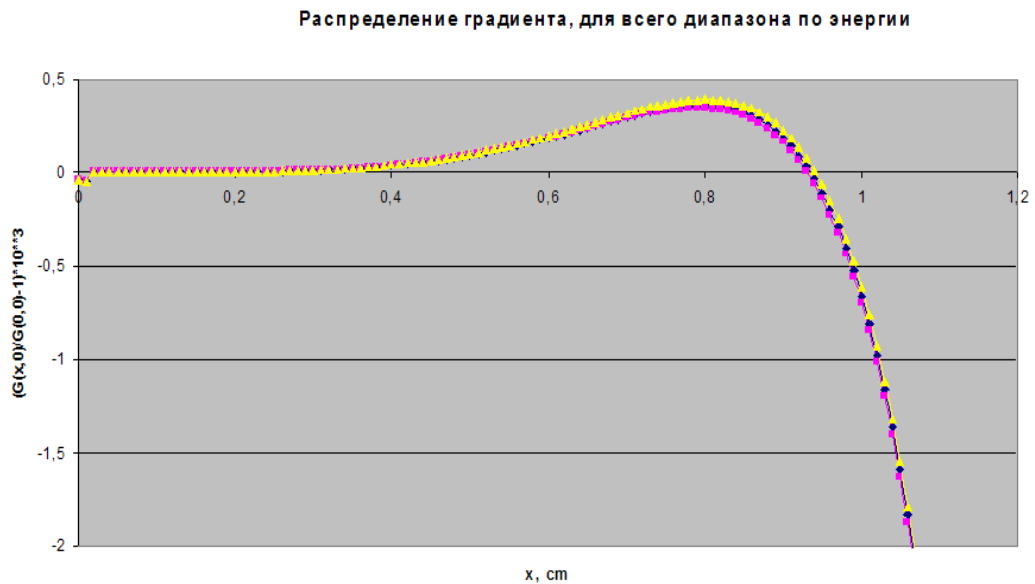


Fig. 3.25 Dependence of the gradient of the lens *SEQ0* (*NEQ0*) on the transversal coordinate for gradients of 11 kG/cm, 9 kG/cm and 5.3 kG/cm.

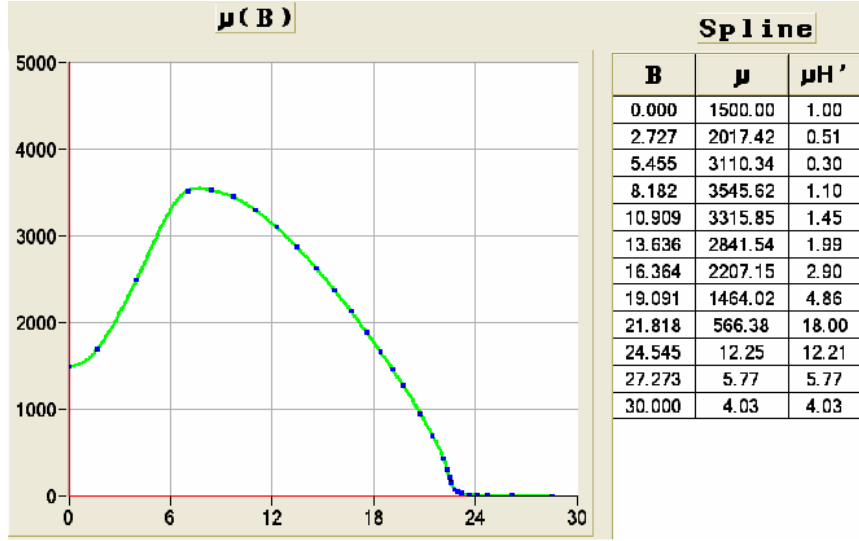


Fig. 3.26 Magnetization curve of the permendure for the yoke of the FF lens.

The excitation coil of the lens is wound of superconducting *NbT* wire of a 1.20×0.75 mm rectangular cross section, manufactured by *Oxford Instruments*. The coil consists of two layers of 7 turns in each. The minimum bend radius is about 7 mm. The coil is wound in a simple flat shape as shown in Fig. 3.27 and then bent into a saddle shape and made monolithic.

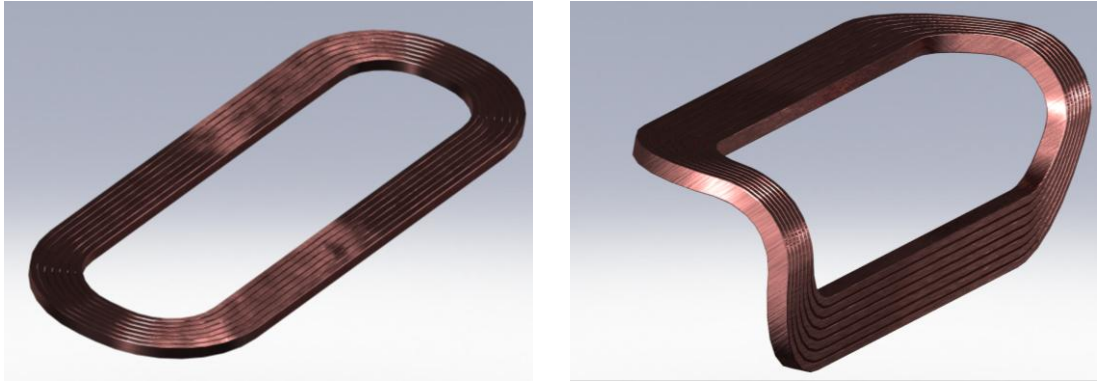


Fig. 3.27 Fabrication of the superconducting coil.

The design of the second (focusing) lens *SEQ1* (*NEQ1*) in the final doublet is similar to that of the first lens; the gradient of the first lens is less, but the aperture is larger. Computation of the magnetic field shows that it is possible to obtain a gradient differing from the ideal one by $\Delta G/G_0 < 10^{-3}$ within the operation aperture $R = 22$ mm.

3.5. Beam-beam effects and luminosity

For flat ($\sigma_y \ll \sigma_x$) electron-positron beams colliding at an arbitrary horizontal angle θ , the luminosity and the shifts of the betatron tunes are determined by the following formulas [11, 12]:

$$L = \frac{\gamma}{2er_e} \cdot \frac{I \cdot \xi_y}{\beta_y},$$

$$\xi_x = \frac{N_p r_e}{2\pi\gamma} \cdot \frac{\beta_x}{\sigma_x^2(1+\phi^2)}, \quad \xi_y = \frac{N_p r_e}{2\pi\gamma} \cdot \frac{\beta_y}{\sigma_x \sigma_y \sqrt{1+\phi^2}},$$

$$\phi = \frac{\sigma_z}{\sigma_x} \cdot \text{tg} \left(\frac{\theta}{2} \right).$$

Here I is the total beam current, N_p is the number of particles in the bunch, ϕ is the Piwinski angle. Thus, it is clear that increasing the luminosity requires raising the total current and ξ_y as well as reducing the vertical beta function at the IP. In so doing, it is necessary to keep in mind that

- 1) Increasing the total current at the expense of the bunch amount (making the inter-bunch distances smaller) may be restricted by the beam interaction effects at parasitic IPs;
- 2) N_p is restricted by the collision effects (ultimate ξ) and the electromagnetic interaction of the beam with the vacuum chamber, which imposes limitations on the minimum bunch length;
- 3) At attempts to make $\beta_y < d$, where d is the length of the region of beam interaction ($d \approx \sigma_z$ for small ϕ), the ultimate ξ_y and luminosity will decrease due to the *hour-glass* effect.

All this makes a substantial increase in the luminosity impossible with the traditional methods.

In March 2006, the Italian physicist Pantaleo Raimondi suggested a fundamentally new scheme of beam collision [10] known as the Crab Waist scheme. Its main feature is a large Piwinski angle ($\phi \geq 10$), obtained by reducing σ_x at the IP (small emittance and β_x), so that the crossing angle θ is still small, about $50 \div 60$ mrad. In this case, the size of the beam intersection region d becomes much smaller than the bunch length: $d \approx \sigma_z / \phi$ for $\phi \gg 1$, which allows an abrupt reduction in β_y and gives a huge gain in the luminosity for the same total current. Additional advantages of this scheme are a small space charge parameter ξ_x and the absence of problems with parasitic IPs because of moving the beams far apart in terms of σ_x .

Another fundamental feature relates to the "crab" sextupoles which are located on both sides of the IP, in places with a certain betatron phase advance. These sextupoles rotate the vertical "waist" of the beam at the IP, which is reflected in the name of the scheme. This rotation gives a small (5 ÷ 10%) gain in the luminosity due to geometrical factor, but their main effect is the strong suppression of the betatron and synchro-betatron coupling resonances [21, 22]. The ultimate value of the parameter ξ_y increases 2-3 times!

This scheme was first tried at the Italian Φ -factory DAΦNE, which increased its luminosity three times; a good agreement between the experimental data and the numerical simulations was achieved [23, 24]. Now the CW scheme is the base of the project of the Italian Super B factory [25] and the Japanese Super KEKB factory.

At large ϕ , the expressions for the shift of the betatron tunes can be rewritten as follows:

$$\xi_x = \frac{2N_p r_e}{\pi\gamma} \cdot \frac{\beta_x}{(\theta\sigma_z)^2}, \quad \xi_y = \frac{N_p r_e}{\pi\gamma} \cdot \frac{\beta_y}{\theta\sigma_z\sigma_y}.$$

It can be seen that a simultaneous increase in N_p and the bunch length leaves ξ_y unchanged and no problems with the high bunch current arise because its length is also growing.

On the other hand, it should be remembered that this scheme requires a fairly specific magnetic structure of the storage device. For example, there is a problem of obtaining a required dynamic aperture (including the energy acceptance), small emittances at high beam currents, etc. As a result, the maximum ξ_y may turn out to be determined not by the collision effects, as is usually the case, but by other factors.

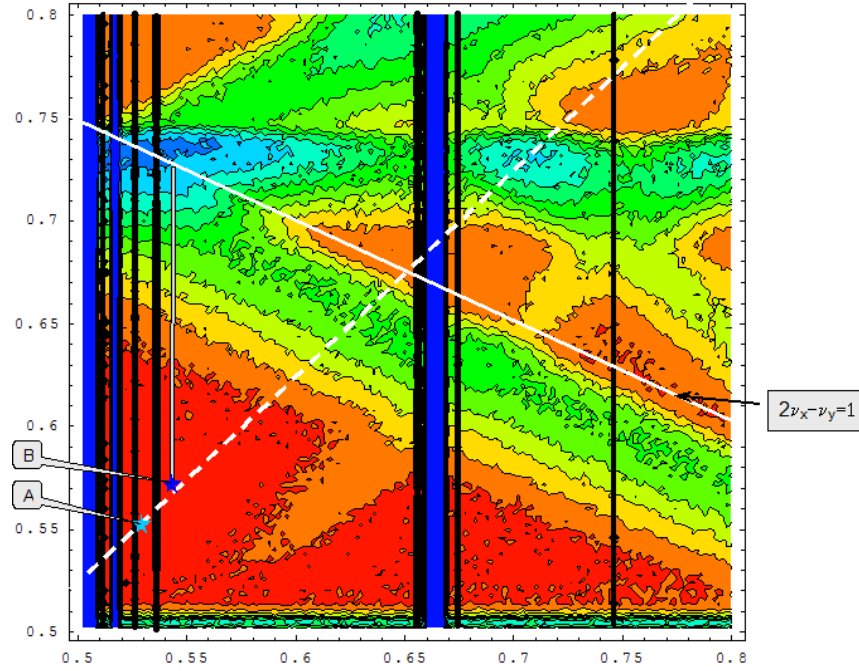


Fig. 3.28 Luminosity as a function of the betatron tunes for $\zeta_y = 0.12$. Low and high luminosity is shown with the dark blue/black and red colors, correspondingly.

To study the BB effects in the Crab Waist scheme, identify the main factors limiting the luminosity, and choose the working point, a numerical simulation was carried out with the LIFETRAC code. A simplified model of the ring was used (a linear structure without betatron coupling). The rated vertical emittance was obtained at the expense of artificially imposed vertical noise. The results of the simulation – luminosity as a function of unperturbed betatron tunes – are shown in Fig. 3.28. In the red region, the luminosity is in the range of $(1.0 \div 1.1) \cdot 10^{35} \text{ cm}^{-2} \text{ s}^{-1}$. Of strong resonances limiting the good area we should note the horizontal synchro-betatron resonances (mainly the synchrotron satellites of the half-integer resonance), which are shown with the vertical blue and black stripes, as well as the low-order coupling resonance of $2\nu_x - \nu_y = 1$, which is shown with the white line. Since the shift of the horizontal tune ζ_x is very small at a large Piwinski angle (the spread of the tunes in the beam being even much smaller [26]), the beam-occupied region in the tune diagram («footprint») has the form of a narrow vertical stripe. This means that the horizontal synchro-betatron resonances do not restrict the luminosity but only the choice of the working point. The luminosity is limited by the resonance of $2\nu_x - \nu_y = 1$. The upper edge of the footprint (small betatron amplitudes) must remain below this resonance, which thus sets limits on ζ_y for every operating point. Therefore, to obtain the maximum luminosity it is necessary to move left and down along the dotted line, towards the half-integer resonance. For example, at the point (0.528, 0.550) (marked A in Fig. 3.28), you can easily get $\zeta_y = 0.3$, which is 2.5 times greater than the calculated value! In this case, the actual betatron tune shift $\Delta\nu_y$ will of course be less, about 0.19, which corresponds precisely to the distance from the resonance. In the simulation, this increase in ζ_y was achieved by simply raising the bunch current. In so doing, the horizontal emittance grew by 20% due to the collision effects; the vertical emittance, by 40%, the specific luminosity, 2.35 times and the "tails" of the equilibrium distribution remained around $10 \sigma_x$ and $15 \sigma_y$.

On the other hand, the nonlinearities of the magnetic lattice of the storage ring taken into account, the spread of the horizontal betatron tunes will be more than just ζ_x . Therefore the choice of a working point cramped between two strong synchro-betatron resonances may be nonoptimal. Point B (0.545, 0.570) looks more attractive. Here the ultimate $\zeta_y \approx 0.24$, and the corresponding footprint is shown in Fig.3.28 with the gray strip, which begins at this point and bears against the resonance line $2\nu_x - \nu_y = 1$.

Fig. 3.29 shows the results of simulation for this operating point with different bunch currents. It can be seen that the vertical size and the specific luminosity vary only slightly with ζ_y , increasing from 0.12 to 0.24, with a sharp jump following.

Increasing the bunch current in the simulation helps one to understand where the limits on the luminosity due to the BB effects are. However, in practice, the maximum bunch current will be limited by other factors: the bunch length, the power of the injector, etc. Another way to increase ζ_y is to reduce the vertical emittance, which also looks problematic since it will lead to a significant decrease in the lifetime of the beams, which is determined by the scattering on the colliding bunch and the intra-bunch scattering (Touschek effect).

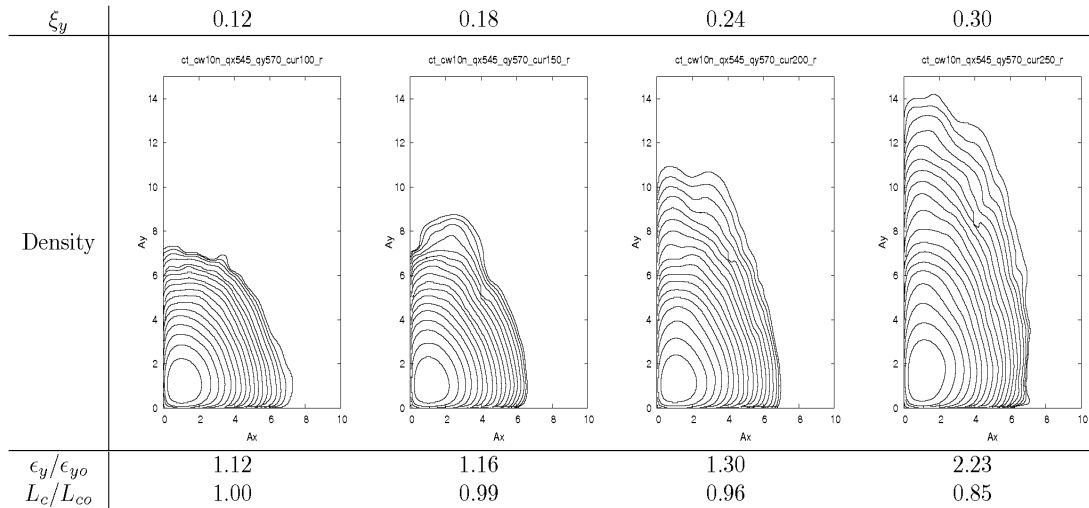


Fig. 3.29 The equilibrium beam distribution in the plane of normalized betatron amplitudes, the vertical emittance, and the specific luminosity in dependence on ζ_y for the working point (0.545, 0.570). The distribution density on adjacent lines of the level differ e times. L_{c0} is the specific luminosity for the nominal parameters ($\zeta_y = 0.12$).

Besides, the choice of the operating point is determined not only by the BB effects but also by the nonlinear structure of the storage ring. The calculations show that, because of the strong nonlinear chromaticity, the dynamic aperture for particles with non-equilibrium energy is small near the half-integer resonance. Therefore it is necessary to raise the betatron tunes. If there is no need to increase the rated ζ_y , which already provides a luminosity of $10^{35} \text{ cm}^{-2}\text{s}^{-1}$, the choice of the betatron tunes becomes much wider: any red dot (see Fig. 3.28) to the right and above point B . The final choice will be made after the end of the optimization of the dynamic aperture.

We can conclude that for the calculated parameters, the collision effects will not have a significant influence on the beam dynamics. The calculated value $\zeta_y = 0.12$ is small and allows varying the operating point in a fairly wide range. If it can be moved closer towards the half-integer resonance, the ultimate ζ_y grows. This opens up the possibility of obtaining higher luminosity.

3.6. Longitudinal polarization at the IP

Spin-polarized electrons arise on the photocathode of the source with energy of 100 keV to 200 keV and then are accelerated to the energy required in the experiment, 1 GeV to 2.5 GeV. A spin manipulator of the source can set any desirable direction of the electron spin at the point of their injection into the ring. It remains to arrange such a closed spin trajectory along the ring circumference that the spin is directed longitudinally at the point of the electron-positron collision.

3.6.1. Closed spin orbit. Spin rotators.

We suggest installing 5 spin rotators – Siberian snakes [27] – on the electron storage ring, each snake rotating the spin through 180° around the longitudinal axis of the accelerator coordinate system. Each snake consists of two SC solenoids separated by a mirror-symmetrical optical system of 7 quadrupole lenses, see Fig.3.30. The total integral of the field of the two solenoids is

$$\int Bdl = \pi B\rho = 26 \text{ T}\cdot\text{m}, \text{ if } E=2.5 \text{ GeV}$$

The transport matrix of the spin rotator, including the solenoids, must comply with the following two conditions: 1) zero 2x2 off-diagonal blocks, 2) spin transparency. Both these requirements are met for a full Siberian snake if [28]

$$T_x = -T_y = \begin{pmatrix} -\cos(2\varphi) & -2r \sin(2\varphi) \\ (2r)^{-1} \sin(2\varphi) & -\cos(2\varphi) \end{pmatrix} = \begin{pmatrix} 1 & 0 \\ 0 & 1 \end{pmatrix}$$

where φ is the angle of spin rotation by one solenoid. For a full snake, $\cos(2\varphi) = -1$. If $\varphi < \pi/2$, the snake is called partial. Unfortunately, it yields to a full one and will not be considered here.

A method of compensation of the solenoid-introduced betatron coupling via inserting an optical system meeting the condition $T_x = -T_y$ between the solenoids was proposed in [29]. A big advantage of this method is no need to use any skew-quadrupoles. In this scheme the solenoid field may vary in a wide range without changing the strength of the quadrupole lenses, including their complete switching off, the coupling remaining zero in this case. Though, if one wants to leave the advance of the betatron phases unchanged throughout the insert, the field gradients in the lens still have to be slightly corrected. The main advantage is that there is no need to rotate the lenses around the longitudinal axis as it is with some alternative schemes of compensation of coupling also considered in [29].

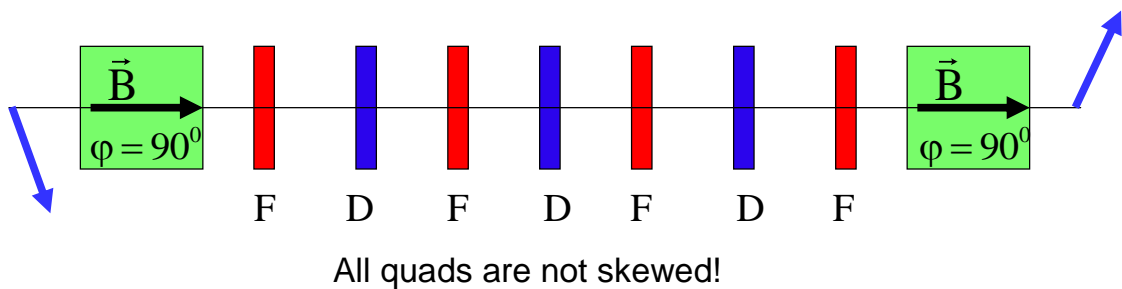


Fig. 3.30 Optical scheme of the spin rotator – the Siberian snake rotating the spin through 180° around the axis of the solenoids.

With an odd number of the snakes the spin in the arcs of the ring lies in the median plane and takes exactly the longitudinal direction in the middle of the arcs between the snakes. It is presented schematically in Fig. 3.31, where the equilibrium direction of the spins – a closed spin trajectory – in the ring with the three snakes evenly placed in azimuth is shown.

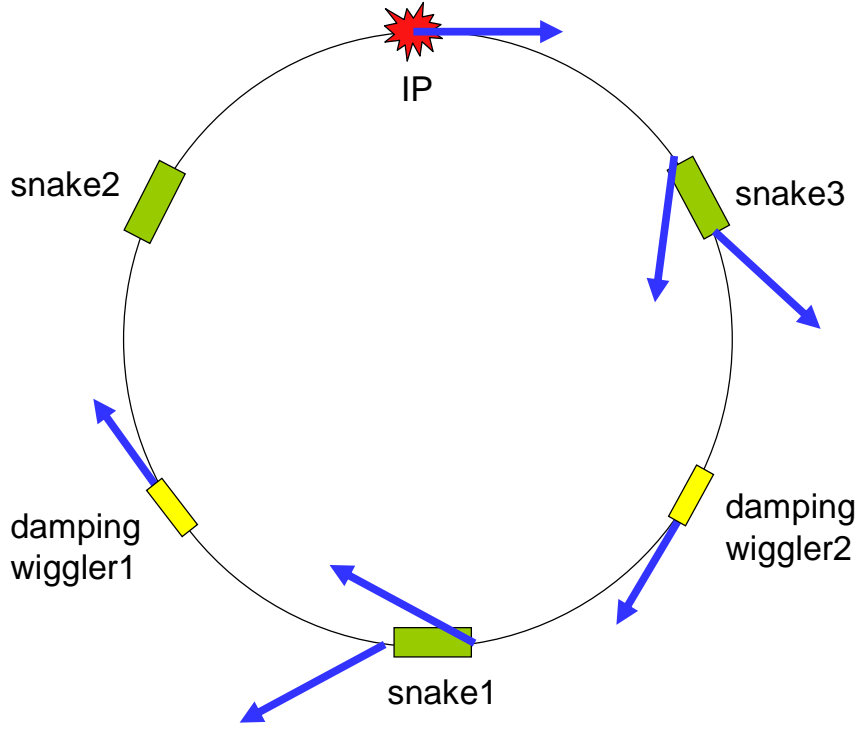


Fig. 3.31 The equilibrium closed spin trajectory in the ring with three Siberian snakes. The depolarizing influence from the damping wigglers is minimal if they are situated in those places where the spin is longitudinal.

3.6.2. Radiative relaxation of spins

The larger the number of the snakes installed on the ring, the greater the depolarization time reached. The depolarization time increases proportionally to the square of the number of the snakes. We chose five snakes providing perfect preservation of the electron beam polarization across the energy range. At low-energy operation it is possible to use a smaller number of snakes. The analytical estimates of the azimuth-averaged squared modulus of the vector of the spin-orbit coupling for a ring with n_{snk} Siberian snakes give the following result:

$$\langle \vec{d}^2 \rangle = \vec{d}^2(0) + \frac{\pi^2}{3} \frac{\nu^2}{n_{snk}^2}$$

$$\vec{d}^2(0) = \frac{\pi^2}{4} \sin^2 \frac{\pi\nu}{n_{snk}}$$

Here \vec{d} is the spin-orbit coupling vector, $\vec{d}^2(0)$ is the squared modulus of it at the minimum point, $\langle \vec{d}^2 \rangle$ is its value averaged over the arc length, and $\nu = E(\text{MeV}) / 440.652$ is the spin frequency. The azimuthal dependence of $\vec{d}^2(\theta)$ for the cases of $n_{snk} = 1$ and $n_{snk} = 3$ for the electron energy $E = 1$ GeV is presented in Fig. 3.32. Knowing the behavior of \vec{d} in the ring, it is easy to calculate the time of the radiation spin relaxation as well as the equilibrium degree of radiation polarization. They are determined from the known formulas by Derbenev and Kondratenko [30]:

$$\xi_{\text{rad}} = -\frac{8}{5\sqrt{3}} \frac{\langle |r|^{-3} \vec{b}(\vec{n} - \vec{d}) \rangle}{\langle |r|^{-3} \left(1 - \frac{2}{9}(\vec{n}\vec{v})^2 + \frac{11}{18}\vec{d}^2 \right) \rangle}$$

$$\tau_{\text{rad}}^{-1} = \frac{5\sqrt{3}}{8} \lambda_e r_e c \gamma^5 \langle |r|^{-3} \left(1 - \frac{2}{9}(\vec{n}\vec{v})^2 + \frac{11}{18}\vec{d}^2 \right) \rangle$$

Here r is the radius of curvature of the orbit in the dipole magnets, \vec{b} is the unit vector directed along the field in these magnets, \vec{n} is the unit vector of the equilibrium spin direction, \vec{v} is the unit vector directed along the velocity, and the rest designations are standard.

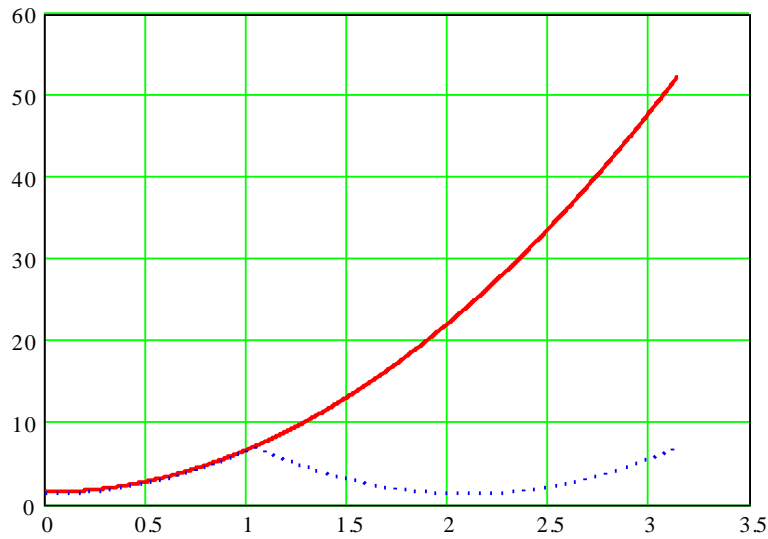


Fig. 3.32 Azimuthal dependence of the squared modulus of the vector of the spin-orbit coupling at the energy $E = 1 \text{ GeV}$ with one and three (dark blue dots) Siberian snakes.

At the $c\tau$ -factory the wigglers are supposed to be used for the regulation of the radiative damping decrements, namely, to maintain the damping time of around 30 ms in the entire energy range of the complex. At low energy the wigglers are turned on for the maximum field, while at the maximum energy near 2.5 GeV the wigglers are completely turned off. When calculating the time of depolarization in the storage ring, it is necessary, of course, to consider the influence of the wigglers on this process. As seen in Fig. 3.33, the contribution of the damping wigglers strongly depends on the place of their location. If they stand in such segments of the ring where the modulus of the spin-orbit coupling is minimal (in the middle of the arc between the two wigglers), their effect is negligible. If they are distributed evenly over the ring, their influence is quite palpable.

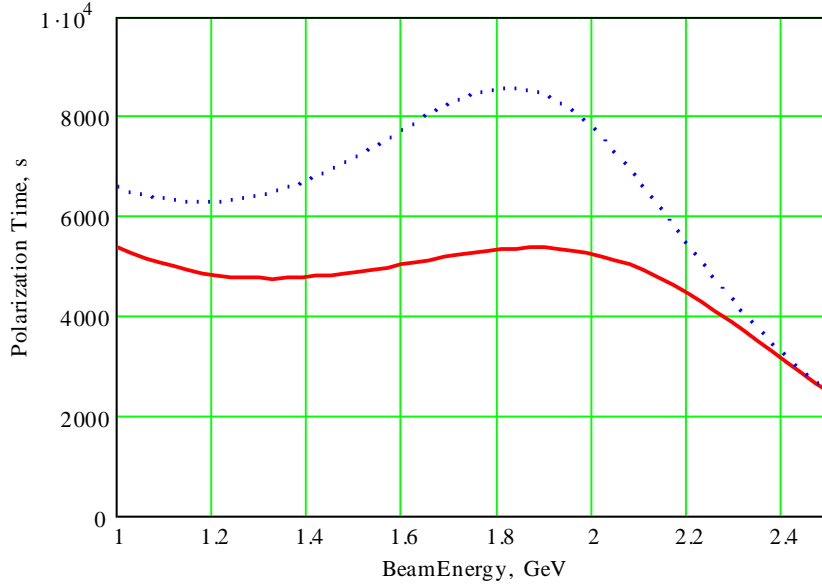


Fig. 3.33 Dependence of the time of spin relaxation on the electron energy in the variant with five Siberian snakes. The solid curve corresponds to the uniform placement of the wigglers over the ring, and the dots show the preferable variant of placing the damping wigglers at points with the minimum modulus of the spin-orbit coupling.

3.6.3. Time-averaged degree of polarization

With the Siberian snakes on the ring, the equilibrium degree of radiative polarization of the beams almost vanishes. This is a positive moment because a definite sign of beam polarization may lead to systematic errors in the analysis of the spin asymmetry of the processes of interest. It is planned to randomly inject several (up to a few hundreds) bunches of polarized electrons into different separatrices and mark all the recorded events with the number of the separatrix they correspond to. The loss of particles occurring mainly due to the bremsstrahlung on the counter beam, of course, must be made up for with the fresh-polarized electrons. As a result, some equilibrium polarization degree determined by the balance of particles surviving in the ring for different times will establish gradually. It is easy to show that the equilibrium polarization degree is equal to

$$\xi = \xi_{beam} \frac{\tau_{rad}}{\tau_{beam} + \tau_{rad}} + \xi_{rad} \frac{\tau_{beam}}{\tau_{beam} + \tau_{rad}}$$

Here $\xi_{beam} = 90\%$ is the degree of polarization of the fresh beam; $\xi_{rad} \approx 0\%$ is the degree of the radiative self-polarization of electrons in the ring; $\tau_{beam} = 1000$ sec is the lifetime of the particles in the ring; τ_{rad} is the time of the radiative polarization of the spins. Fig. 3.34 presents the plots of the time-averaged degree of electron beam polarization for 1, 3, and 5 snakes. These results were obtained analytically and confirmed by computations with the ASSPIRIN program [31, 32]. It is seen from the figure that the variant with 5 snakes ensures a polarization degree of about 80% across the accelerator energy range.

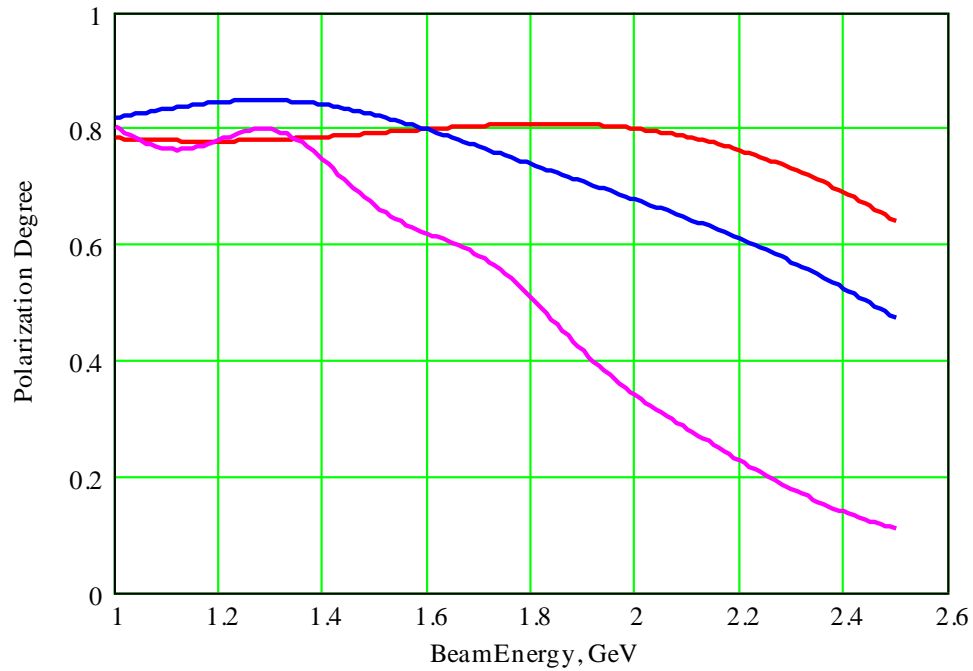


Fig. 3.34 Time-averaged degree of electron polarization in the ring of the c-tau factory for 1, 3, and 5 snakes.

3.6.4. Technical aspects of the realization of the spin rotators

A set of two superconducting solenoids and seven quadrupole lenses should be created for each of the spin rotators. One solenoid is 2 m long and has a maximum field of 6.5 Tesla and a 4-cm aperture. It seems that a solenoid with such parameters can be cooled with a three-stage cooler and placed in just a vacuum cryostat without liquid helium. Such experiments using indirect cooling of small superconducting devices are currently under way.

The total length of the Siberian snake is about 10 meters, or about 1.5% of the entire perimeter. All the quadrupole lenses have the same specifications as the main lenses of the ring.

We have investigated the issue of the field of tolerances for the deviation of the gradients of the lenses from the nominal values. No too severe restrictions on the precision of control over the currents of the lenses were found. In fact, deviations of the field in the lenses and solenoids of up to 10% lead to no substantial increase in the vertical emittance.

3.7. Life time of the beams

The life time of the beams depends strongly on the particle loss due to their scattering on the counter beam at the IP (Fig.3.35). This influence is proportional to the luminosity of the collider

$$\frac{dN}{dt} = -\sigma \cdot L,$$

where σ is the cross section of the process and L is the luminosity. Naturally, the role of this influence increases with the luminosity.

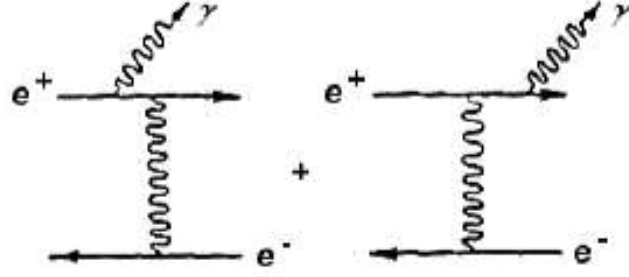


Fig. 3.35 Inelastic scattering of the particles of the colliding beams.

If the luminosity is considered constant, the dependence of the number of the particles on the time may be estimated approximately as

$$N(t) \approx N_0 e^{-\Delta t \frac{\sigma L}{N_0}}.$$

It is necessary to distinguish between elastic scattering, $e^+e^- \rightarrow e^+e^-$, and single bremsstrahlung from one particle in the field of another particle, $e^+e^- \rightarrow e^+e^-\gamma$. The cross section of the elastic process that leads to loss of a particle if the angle of its deviation exceeds the acceptance of the accelerator is in this case more than one order of magnitude smaller than the bremsstrahlung cross section.

A standard quantum electrodynamics (QED) calculation of the E_γ -differential cross section of single bremsstrahlung gives the following:

$$d\sigma_{cl} = \frac{16\alpha}{3} r_0^2 \frac{dy}{y} \left[1 - y + \frac{3}{4} y^2 \right] \left[\ln \left(\frac{4\gamma^2(1-y)}{y} \right) - \frac{1}{2} \right],$$

where $y = E_\gamma / E_b$, E_b is the beam energy, and r_0 is the classical electron radius. Small momentum transfers corresponding to large impact parameters contribute to single bremsstrahlung. This makes the process cross-section sensitive to various macroscopic effects. As was shown in experiments on VEPP-4, the restriction of the impact parameters by the transverse dimension of the beam is the most important.

Single bremsstrahlung can be considered as the scattering of virtual photons accompanying an electron on a counter electron. Virtual photons with an energy ω fill a disk of the radius $\rho \sim \gamma / \omega$. The main contribution to the bremsstrahlung cross-section comes from the photons with the energy $\omega \sim E_\gamma / 4\gamma^2$, for which the effective "disk" has a characteristic radius

$$\rho \sim \frac{4\gamma^2}{E_\gamma} \approx 4 \text{ mm} \quad \text{at} \quad E_\gamma / E_b = 0.01.$$

Since the transverse beam size is $\ll 4$ mm, not all virtual photons encounter electrons, and a standard QED calculation gives an overestimated cross section. The impact parameters of the process were allowed for correctly in [33, 34], and the results of these studies are used below to estimate the lifetime of the beams at the $c\tau$ -factory. The single-bremsstrahlung cross-section obtained in the standard manner and subject to the amendments is shown in Fig. 3.36.

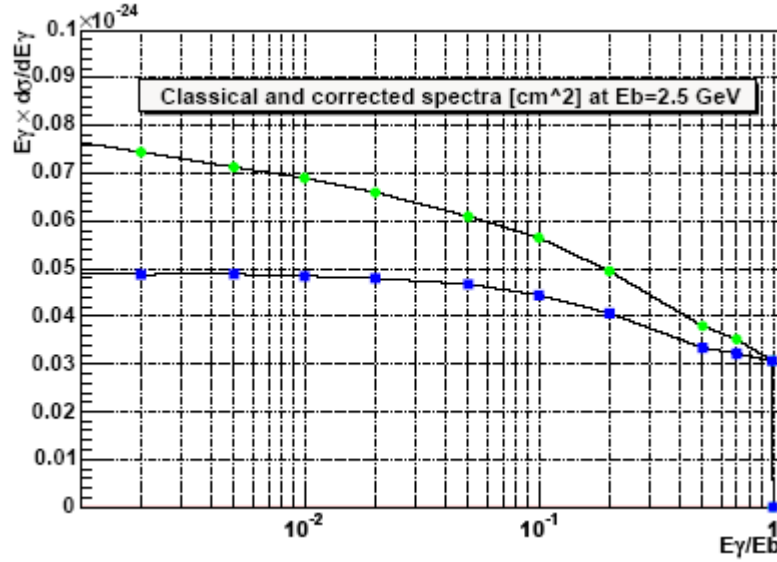


Fig. 3.36 Bremsstrahlung cross-section (to one side) at $E_b = 2.5$ GeV, $\sigma_y = 0.39$ μm and $\sigma_x = 14$ μm . The upper curve is the result of a standard QED calculation; the lower one was obtained with the impact parameters taken into account.

The rate of the particle loss and the beam life time determined by single bremsstrahlung, calculated for the $c\tau$ -factory parameters subject to the restriction of the impact parameters are shown in Fig.3.37. The minimum life time in the energy range of $\sim 1.8 \div 2.5$ GeV is 1600 seconds.

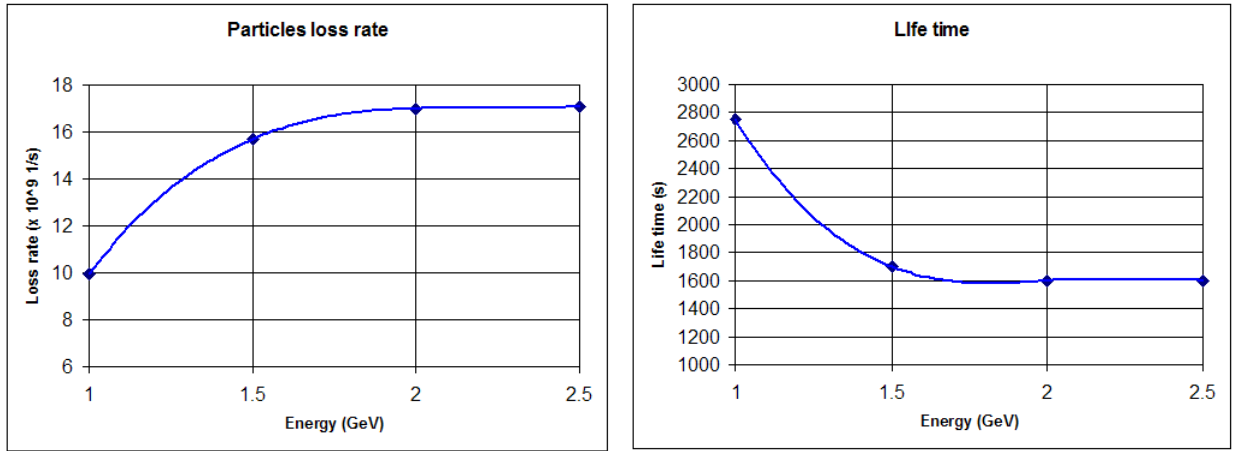


Fig. 3.37 Particle loss (left) and beam life time (right) for single bremsstrahlung.

For low beam emittance and the fairly large bunch intensity it is expected that the intra-bunch scattering of particles (Touchek effect), which is determined as

$$\tau_T^{-1} = \frac{1}{N} \frac{dN}{dt} = \frac{Nr_0^2 c}{8\pi\sigma_x\sigma_y\sigma_z} \frac{\lambda^3}{\gamma^2} D(\xi),$$

where λ is the energy aperture

$$\xi = \left(\frac{\Delta E / E}{\gamma} \right)^2 \frac{\beta_x}{\varepsilon_x},$$

and the $D(\xi)$ function is determined as [36]

$$D(\xi) = \sqrt{\xi} \left(\ln \left(\frac{1}{1.78\xi} \right) - \frac{3}{2} \right)$$

will be one more important effect influencing the life time of particles at the $c\tau$ -factory.

The energy aperture, the size of which influences the ‘‘Touchek’’ life time very much, is chosen as the least of the RF acceptance and the energy dynamical aperture, the latter being determinative in this case.

The life time determined by the intra-bunch scattering was modeled for a realistic accelerator structure using a modified Piwinsky algorithm [37]. The results of the modeling at energy of 2 GeV are presented in Fig.3.38.

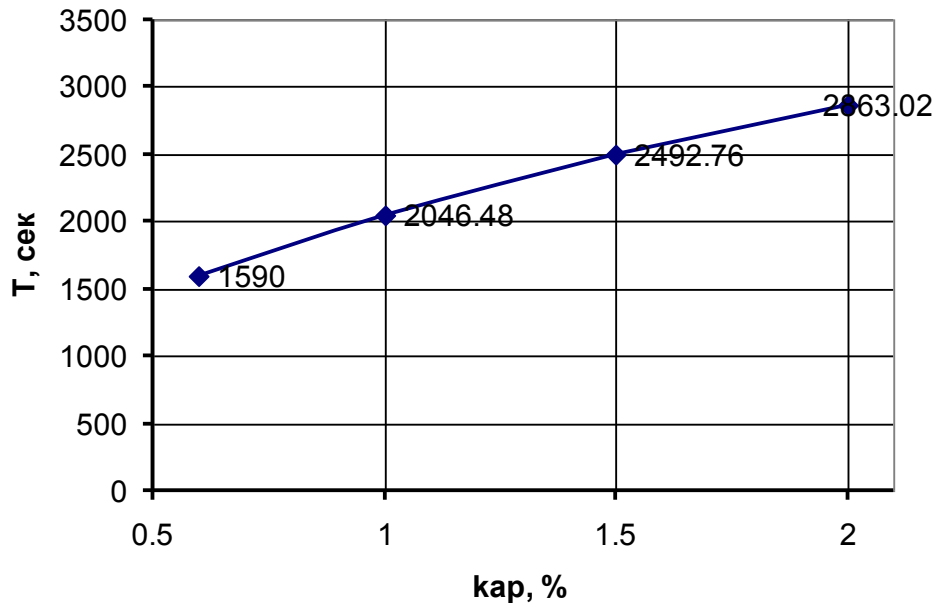


Fig. 3.38 Life time determined by the intra-bunch scattering as a function of the betatron coupling for energy of 2 GeV.

3.8. Collective effects

3.8.1. Collective effects

The interaction of an intense beam of charged particles with the electromagnetic fields induced by it in a vacuum chamber (wake-fields) leads to various collective effects in the beam dynamics. These effects depend on the beam intensity and manifest themselves with a large number of particles in the beam. The most significant result of the collective effects is the instability of beam motion. When the resonance conditions are met, small deviations in the beam position or energy can increase because of the beam interaction with the wake-fields. Such positive feedback leads to instability of the oscillations and, consequently, beam loss or degradation.

In the frequency domain, the beam interaction with the components of the vacuum chamber through the wake-fields is described with the frequency-dependent coupling impedances. The presence of sections with narrow-band impedance (e.g. the parasitic higher modes of the accelerating cavities) in the accelerator may give rise to multi-bunch instability, and the broadband impedance can cause single-bunch instability of the beam. The foundations of the theory of collective effects, instabilities, and coupling impedances are given in [38, 39, 40].

The vacuum chamber of accelerator as a whole is usually represented as a broadband impedance obtained by summing the broadband impedances of all the components of the

chamber. The broadband impedance can be assumed additive since the wake-fields decay rapidly, and the interference of the beam-excited wake-fields in different components of the vacuum chamber can be ignored in practice. The value of the total broadband impedance is used to estimate the single-bunch stability of the beam motion and is a criterion of the quality of the vacuum chamber design and manufacturing.

For estimating the maximum allowable coupling impedances of the collider to design, it would be useful to consider the experience of the existing B-factories – KEKB and PEP-II. It makes sense to compare the parameters of the storage rings, the beam energy of which is close to energy of 2.5 GeV, which was chosen for the $c\tau$ -factory. Those are the KEKB LER with energy of 3.5 GeV and PEP-II LER with energy of 3.1 GeV. The energy of the KEKB HER and PEP-II HER storage rings is 8 GeV and 9 GeV, respectively, which is significantly higher than the design energy of the $c\tau$ -factory under consideration.

The main parameters of KEKB LER, PEP-II LER and $c\tau$ -factory that are of interest for the analysis of the collective effects as well as the results of the instability estimates are presented in Tables 1 and 3 (see Attachment).

3.8.2. Beam lengthening

The beam-induced electromagnetic fields change the shape of the accelerating RF field that affects the beam, which results in the distortion of longitudinal distribution of the particles and beam lengthening, while the energy spread does not change. The beam lengthening caused by the potential well distortion is described with the following equation:

$$\left(\frac{\sigma_s}{\sigma_{s0}}\right)^3 - \frac{\sigma_s}{\sigma_{s0}} + I_b \frac{\alpha \operatorname{Im}(Z_{\parallel}/n)_{\text{eff}}}{\sqrt{2\pi} \frac{E}{e} v_s^2} \left(\frac{R}{\sigma_{s0}}\right)^3,$$

where I_b is the beam current, $\sigma_{s0} = \frac{c\alpha}{v_s \omega_0} \frac{\sigma_E}{E}$ is the bunch length at a zero current, $\frac{\sigma_E}{E}$ is the relative energy spread, R is the mean radius of the accelerator, α is the momentum compaction factor, ω_s is the synchrotron frequency (in units of the revolution frequency ω_0). The effective impedance $(Z_{\parallel}/n)_{\text{eff}}$, which is often used to estimate the beam stability, is the weighted normalized impedance Z_{\parallel}/n averaged over the beam frequency spectrum [44]. There is an approximate relation between the low-frequency broad-band impedance and the effective one, which depends on the rms bunch length. For short bunches, if the rms bunch length $\sigma_t = \sigma_s/c$ is by far less than $1/\omega_c$, where $\omega_c = c/b$ is the characteristic frequency of the impedance (b is the characteristic transverse dimension of the vacuum chamber), we have $(Z_{\parallel}/n)_{\text{eff}} \approx \omega_c \sigma_t (Z_{\parallel}/n)_{\text{BB}}$, while for long bunches, i.e. if $\sigma_t > 1/\omega_c$, it may be considered that $(Z_{\parallel}/n)_{\text{eff}} \approx (Z_{\parallel}/n)_{\text{BB}}$.

If the beam current exceeds a threshold value, the interaction of the beam with the longitudinal impedance leads to microwave instability of the longitudinal motion. Above the instability threshold, increase in the beam current is accompanied by growth both in the longitudinal dimension and in the beam energy spread. For a relativistic beam, the peak value of the threshold bunch current I_p can be estimated using the following formula [45, 46]:

$$I_p \leq \frac{\alpha}{|Z_{\parallel}/n|} \frac{E}{e} \left(\frac{\Delta p}{p}\right)_{FWHM}^2,$$

where $\frac{\Delta p}{p} = \frac{\gamma^2}{\gamma^2 - 1} \frac{\Delta E}{E}$ is the width of the particle distribution throughout the longitudinal momentum, which is equal to the energy spread $\frac{\Delta E}{E}$ for relativistic beams. For a bunch with Gaussian density distribution and the rms length ω_s , the relation of peak bunch current I_p and the average current I_b is:

$$I_p = \frac{\sqrt{2\pi R}}{\sigma_s} I_b.$$

The average threshold current of the microwave instability is determined by the following expression [47]:

$$I_b \leq \frac{\sigma_{s0}}{R} \frac{\sqrt{2\pi\alpha} \frac{E}{e}}{|Z_{\parallel}/n|_{\text{eff}}} \left(\frac{\sigma_E}{E} \right)^2. \quad (3.15)$$

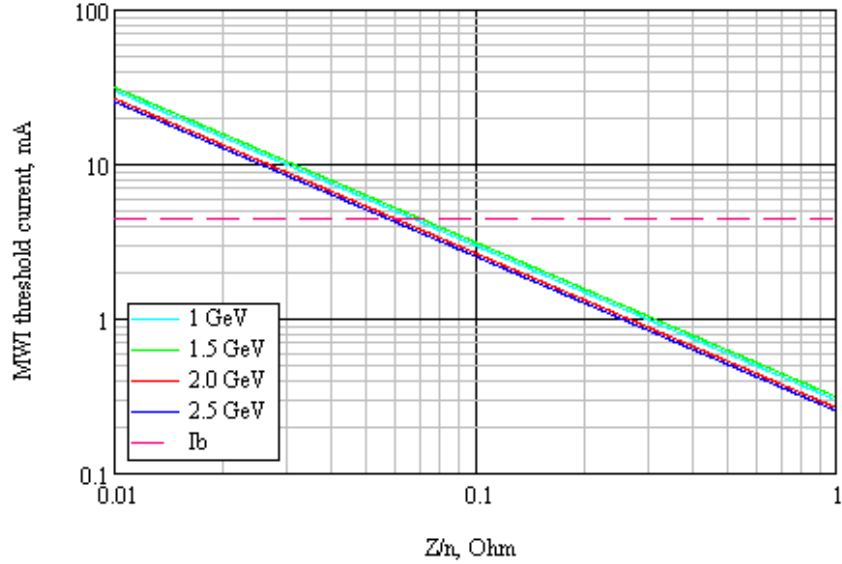


Fig. 3.39 The average threshold current of microwave instability

Fig. 3.39 shows microwave instability threshold current versus the normalized longitudinal impedance. It can be seen that the design bunch current of 4.4 mA will not exceed the instability threshold at normalized impedance less than 70 milliohms. For comparison, the KEKB LER threshold current calculated by formula (3.15) using parameters from Table 1 is 0.1 mA (the working bunch current is 0.5 mA); the PEP-II LER threshold current is 3 mA (the bunch current is 1.3 mA).

Above the threshold of microwave instability, the bunch lengthening as a function of the current is described for a relativistic electron or positron beam with the Gaussian distribution of linear density by the following cubic equation [42, 43]:

$$\left(\frac{\sigma_s}{R} \right)^3 = I_b \frac{\alpha}{\sqrt{2\pi} \frac{E}{e} v_s^2} \left(\left| \frac{Z_{\parallel}}{n} \right|_{\text{cr}} + \left| \frac{Z_{\parallel}}{n} \right|_{\text{eff}} \right),$$

where $\left| \frac{Z_{\parallel}}{n} \right|_{\text{cr}}$ is the impedance value at the critical frequency $\omega_c = c/b$, which mainly determines the turbulent bunch lengthening. Fig.3.40 shows the plots of the bunch length as a function of the bunch current for three values of the normalized longitudinal impedance at energy of

2 GeV and the fixed accelerating voltage $U_{RF}=0.99$ MV. It should be noted that the KEKB LER bunch stretching is about 20% at the working current.

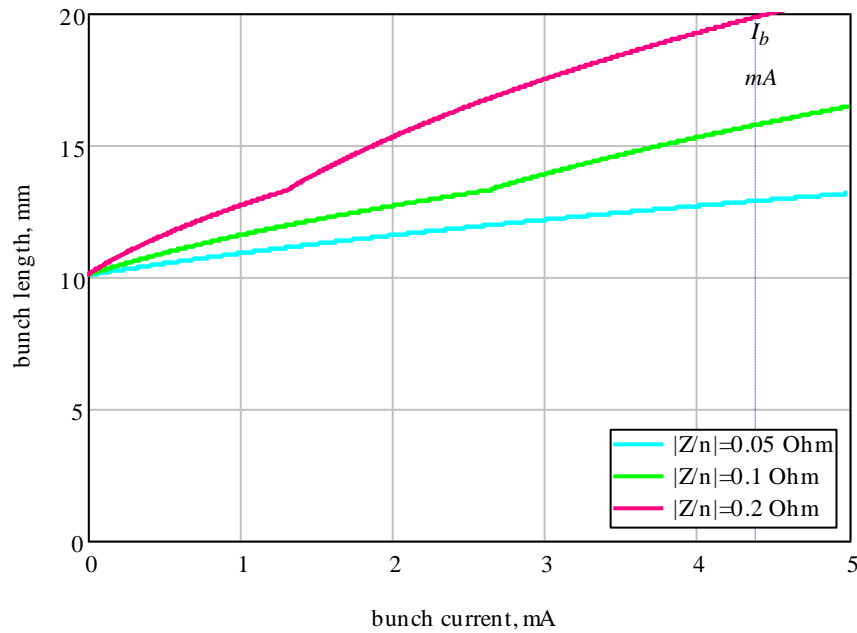


Fig. 3.40 Bunch lengthening as a function of the current.

If it is necessary to keep the longitudinal beam size at any current, the accelerating RF voltage should be increased in order to compensate the bunch lengthening, see Fig. 3.41. One can see the undesirability of exceeding considerably the microwave instability threshold because it leads to a significant increase in the RF voltage required for the bunch lengthening compensation.

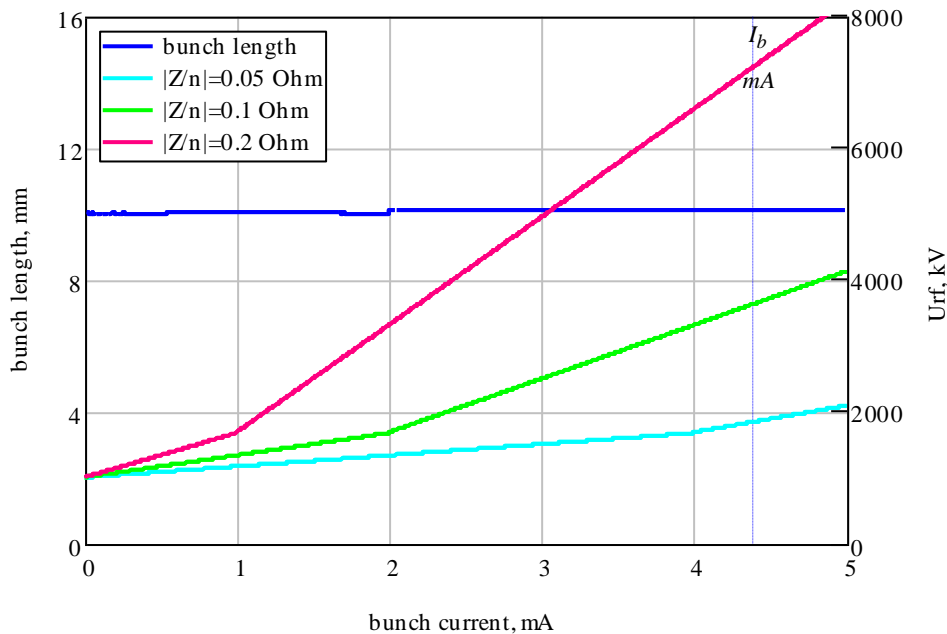


Fig. 3.41 Compensation of the bunch lengthening, $E=2$ GeV.

3.8.3. Coherent energy loss

The real part of longitudinal impedance causes coherent loss of the beam energy that is in quadratic dependence on the beam charge [39]:

$$\Delta E = -k_{\parallel} q^2. \quad (3.16)$$

The coefficient of proportionality k_{\parallel} is called the longitudinal loss factor. It depends on both the properties of the vacuum chamber that are characterized by the impedance Z_{\parallel} and on the longitudinal beam density distribution λ :

$$k_{\parallel} = \frac{1}{\pi} \int_0^{\infty} \text{Re } Z_{\parallel}(\omega) |\lambda(\omega)|^2 d\omega,$$

where $Z_{\parallel}(\omega)$ is the total broadband longitudinal impedance of the chamber and $\lambda(\omega)$ is the Fourier transform of the beam density distribution $\lambda(t)$. Similarly to the loss caused by synchrotron radiation, the coherent energy loss is compensated in the accelerating RF cavities at each beam turn.

Fig. 3.42 shows the graphs of the coherent energy loss as a function of the beam current at 2 GeV, the fixed accelerating voltage $U_{\text{RF}}=0.99$ MV (a) and at the fixed bunch length $\sigma_s=10$ mm (3.16).

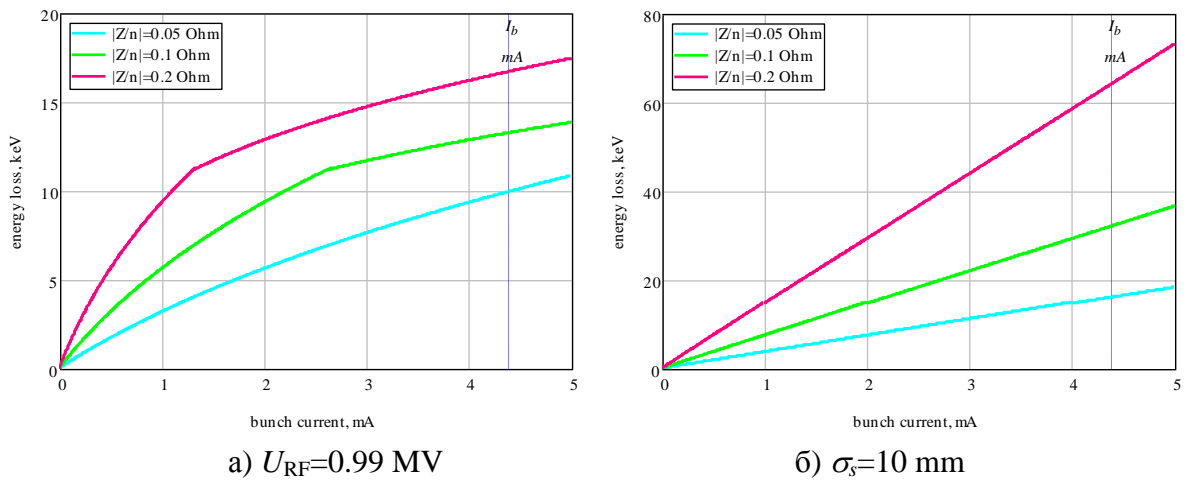


Fig. 3.42 Coherent energy loss, $E=2$ GeV.

3.8.4. TMC instability (fast head-tail)

The resonant interaction between the beam and the short-lived transverse wake-fields, which is characterized by the transverse broadband impedance, causes the instability of the transversely-coupled modes (transverse mode coupling, TMC, or fast head-tail). The wake fields induced by the head part of the bunched beam affect the particles of its tail (head-tail-effect). Due to the synchrotron oscillations, the head and the tail of the beam periodically interchange; when the resonance conditions are met, there occurs an unlimited increase in the amplitude of betatron oscillations, which causes losses of the beam particles till the threshold intensity.

For a vacuum chamber of circular cross section, the relation of longitudinal and transverse dipole impedances is described by the following formula (a consequence of the Panofsky-Wenzel theorem):

$$Z_{\perp} = \frac{2R}{b^2} \frac{Z_{\parallel}}{n},$$

where b is the chamber radius. This formula can also be used for rough estimates in case of a chamber of variable cross section if b is set equal to the average half-height of the chamber.

The interaction of the beam with the reactive part of transverse impedance leads to the coherent shift of betatron tunes. At low currents this shift depends linearly on the beam current [38]:

$$\frac{\Delta\nu_\beta}{\Delta I_b} = \frac{\sqrt{2\pi R} \langle \text{Im} Z_\perp \beta \rangle}{\sigma_s \frac{8\pi E}{e}}, \quad (3.17)$$

where $\langle \text{Im} Z_\perp \beta \rangle$ is the total broadband reactive impedance weighted by the beta function. The coherent shift of the vertical betatron tune of the $c\tau$ -factory, computed by formula (3.17), is $\Delta\nu_y/\Delta I_b = -0.36 \text{ A}^{-1}$ at $E = 2 \text{ GeV}$, $Z_\parallel/n = 0.1 \text{ Ohm}$, and $Z_\perp = 39 \text{ kOhm}$. For comparison, the coherent shift of the vertical betatron tune of the KEKB LER is $\Delta\nu_y/\Delta I_b = 4.2 \text{ A}^{-1}$ (measurement) and of the PEP-II LER, $\Delta\nu_y/\Delta I_b = 0.23 \text{ A}^{-1}$ (calculation).

The threshold current of the TMC instability can be estimated from the coherent shift of the betatron tune in (3.17):

$$I_b \leq \frac{\sigma_s}{\sqrt{2\pi R} \langle \text{Im} Z_\perp \beta \rangle} \frac{8\pi E}{e} \nu_s, \quad (3.18)$$

Fig.3.43 shows the graphs of the threshold current of the TMC instability, (3.18), in dependence on the normalized longitudinal impedance under the assumption that the transverse impedance is proportional to the longitudinal one, in accordance with the Panofsky-Wenzel theorem. For the KEKB LER the threshold current is $I_{\text{th}} = 1.5 \text{ mA}$ at $Z_\perp = 99 \text{ kOhm}$, for the PEP-II LER $I_{\text{th}} = 32.6 \text{ mA}$ at $Z_\perp = 22.5 \text{ kOhm}$.

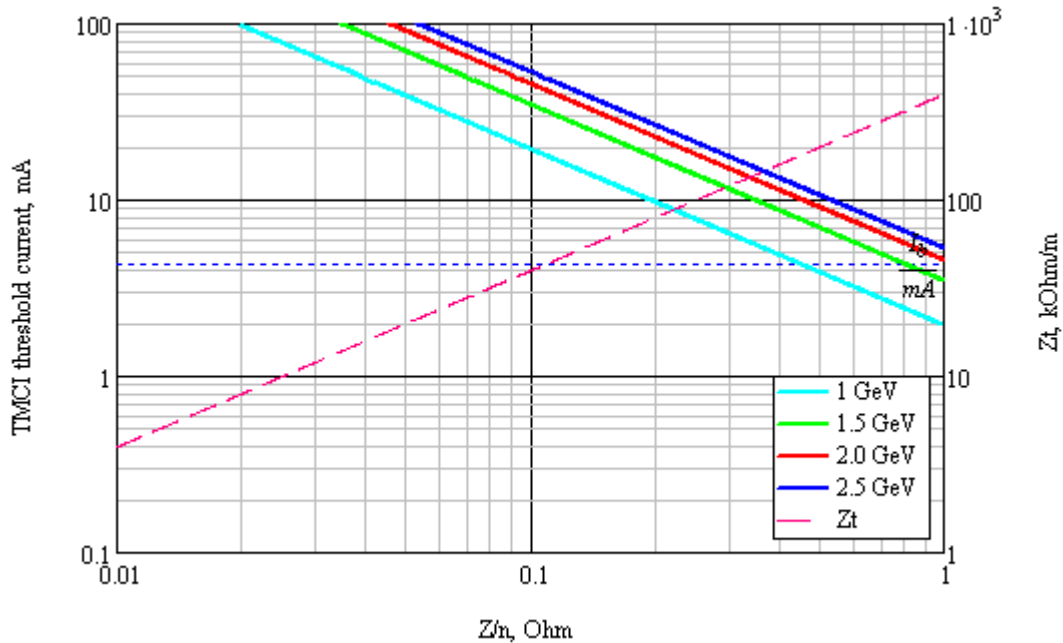


Fig. 3.43 . The threshold current of the TMC instability.

3.8.5. Longitudinal multi-bunch instability

The interaction of the beam with the high-order modes (HOMs) of the accelerating RF cavities (narrowband impedance) leads to excitation of long-lived wake-fields, the influence of which on next bunches may cause longitudinal instability in the multi-bunch mode [48, 49, 50]. If N_b bunches are uniformly distributed over the perimeter of the accelerator, the n th oscillation mode is excited when the resonance condition

$$\omega_r^{HOM} = (pN_b + n + \nu_s)\omega_0,$$

is met, where p is an integer and ν_s is the synchrotron tune. The impedance of every longitudinal mode can be written as

$$Z_{\parallel}(\omega) = \frac{R_s^{HOM}}{1 + iQ \left(\frac{\omega}{\omega_r^{HOM}} - \frac{\omega_r^{HOM}}{\omega} \right)},$$

Since the impedance of each high-order mode is characterized by the corresponding resonance frequency ω_r^{HOM} , shunt resistance R_s^{HOM} and quality factor Q , the instability rise time should be estimated separately for each mode:

$$\frac{1}{\tau} = \frac{\alpha N_b I_b}{4\pi v_s} \cdot \frac{R_s^{HOM} \omega_r^{HOM}}{E}. \quad (3.19)$$

Here I_b is the current of one bunch.

For the motion to be stable, the characteristic time of the radiation damping of the longitudinal oscillations must be less than the rise time of (3.19) for any mode in the operating range of the beam current. Taking the radiation damping into account, we can formulate the stability condition limiting the $R_s^{HOM} \omega_r^{HOM}$ value for any HOM of the RF cavities:

$$R_s^{HOM} \omega_r^{HOM} \leq \frac{1}{\tau_s} \frac{4\pi v_s}{\alpha N_b I_b} \frac{E}{e}.$$

For the $c\tau$ -factory, $R_s^{HOM} \omega_r^{HOM} \leq 10^{13}$ Ohm at $E = 2$ GeV, $N_b = 390$, and $I_b = 4.4$ mA

3.8.6. Transverse multi-bunch instability

The transverse narrow-band impedance of the high-order modes of RF cavities may cause the transverse multi-bunch instability, the rise time of which can be estimated using a formula similar to (3.19) [49]:

$$\frac{1}{\tau} = \frac{\beta_{RFC} \omega_0 N_b I_b}{4\pi \frac{E}{e}} \cdot R_{s\perp}^{HOM},$$

where $R_{s\perp}^{HOM}$ is the shunt resistance of the transverse mode and β_{RFC} is the beta function at the cavity location. The resonance condition for the n th oscillation mode excitation looks as follows:

$$\omega_r^{HOM} = (pN_b + n + \nu_\beta) \omega_0, \quad (3.20)$$

Taking the radiation damping into account, we can also formulate the stability condition limiting the $R_{s\perp}^{HOM}$ value for any high-order mode of the cavities:

$$R_{s\perp}^{HOM} \leq \frac{1}{\tau_\perp} \frac{4\pi \frac{E}{e}}{\beta_{RFC} \omega_0 N_b I_b}.$$

For the $c\tau$ -factory $R_{s\perp}^{HOM} \leq 13$ kOhm at $E = 2$ GeV, $N_b = 390$, $I_b = 4.4$ mA

Besides the high-order modes of the RF cavities, the transverse multi-bunch instability may be excited due to beam interaction with the resistive impedance of the vacuum chamber walls (resistive wall) at the frequencies (3.20). The instability rise time can be estimated as follows [51]:

$$\frac{1}{\tau} = \frac{\langle \beta \rangle \omega_0 N_b I_b}{4\pi \frac{E}{e}} \sum_{p=-\infty}^{\infty} \text{Re} Z_{\perp rw}(\omega_{np}),$$

The frequency dependence of the resistive-wall impedance of a cylindrical vacuum chamber with a radius b and a length L is described by the following expression:

$$Z_{\perp rw} = \frac{\pi^2}{12} (1+i) \frac{L}{2\pi} \frac{Z_0 \delta_s}{b^3},$$

where $Z_0 = 120\pi$ Ohm is the free space impedance and $\delta_s = \sqrt{\frac{2\rho}{\mu\omega}}$ is the skin depth. Thus, the

low-frequency impedance is the most dangerous as concerns the beam stability. For the $c\tau$ -factory the minimum time of the rise time of transverse multi-bunch instability is estimated as $\tau \approx 30$ ms at the frequency $(\nu_y + 1)f_0 \approx 12$ MHz at $E = 2$ GeV, $N_b = 390$, and $I_b = 4.4$ mA

3.9. Stabilization of the beam parameters and the feedback systems

3.9.1 Goals of stabilization

Ensuring the efficient operation of lepton colliders and synchrotron light sources always imposes high demands on the stability of beam parameters. The disturbing factors, the influence of which may reduce the effectiveness of the accelerator include: field deviation in the magnets, alignment errors, seismic vibration, thermal expansion of the magnets and of the accelerating RF cavities, the temperature drift of parameters as well as other dynamic effects. Completely self-automated control of such key beam parameters as the orbit, betatron tunes, coupling factor, chromaticity, energy, etc. with continuous correction of the perturbation introduced by the above factors becomes essentially an integral part of the control systems of modern accelerators.

The diversity of the modern feedback systems results from the variety of requirements to the feedback parameters in accelerators of different types. Let consider the basic principles of construction of systems for stabilization of beam parameters [52]. Requirements to the stability depend on the properties and quality of beams used in experiments. The beam stability in the collider is a necessary condition for the luminosity optimization in high energy physics experiments. Just as in synchrotron radiation sources [53], the orbit stabilization is necessary to minimize the emittance and to provide stable beam convergence at the IPs. Besides the orbit, the feedback system is used to stabilize the betatron tunes so that to prevent crossing of the betatron resonances during acceleration, which may cause loss of beam particles.

Various disturbances affecting the beam orbit, betatron tunes, betatron coupling, chromaticity and energy can be divided into three groups according to their sources:

1. External perturbations: changes in the ambient temperature and the atmospheric pressure; mechanical movement of soil caused by seismic activity, tidal waves and human activity (industry, transport). These disturbances are transmitted into the particle beam mainly through the quadrupoles, the beam focusing in which depends on the transverse displacements.

2. Intrinsic perturbations in the accelerator: variation of fields in the magnets, the noise caused by the flows of cooling fluids, the vibration of air pumps, the eddy currents.

3. Failures of individual elements, which are important for large machines, where failure of one of tens or even hundreds of correcting magnets can stop the experiment for the time of repair.

The characteristic time scale of the perturbations may be long-term (a few months to several days), medium (days or hours) or short-term (hours to milliseconds). The applicability of feedbacks correcting slow beam perturbations is eventually limited by the thermal drift, the noise and the systematic errors of the measuring and correcting circuits. Because of the beam sensitivity to the thermal drift, in the modern machines it is necessary to stabilize not only the

orbit but also the temperature of the experimental hall, the accelerator tunnel, the vacuum chamber and the cooling water within ± 0.1 °C.

External disturbances, beam parameters and the strength of the correctors are functions of time. Therefore, designing feedback systems is often accompanied by a separate analysis of the scheme for correction of deviations of beam parameters from the desired values for a given constant perturbation (space domain) and of time-dependent (time domain) processes describing the operation of the system in real time. Such a separation allows making the system operation more flexible, especially at possible failures of individual elements when quick adjustment of the feedback parameters is required.

3.9.2 Correction algorithms

For most accelerators, the influence of the correcting elements on such parameters as orbit, betatron tune, betatron coupling, chromaticity and energy can be considered linear in the first approximation; the matrix formalism can be used for calculating the correction. The relation of the measured beam parameters and the corrective action in the linear approximation is described with the following matrix equation:

$$\vec{x} = \mathbf{R}\vec{f}^3, \quad (3.21)$$

where $\vec{x} = (x_1, \dots, x_N)$ is the beam parameter vector measured with N pickups; $\vec{f} = (f_1, \dots, f_M)$ is the vector of M corrective actions; \mathbf{R} is the response matrix, the elements R_{ij} of which describe the response of the i th pickup to a variation in the strength of the j th corrector. So, in case of correction of a closed beam orbit, \vec{x} is the set of orbit deviations measured with beam position monitors and \vec{f} are the currents of the dipole magnet correctors.

A space-domain algorithm of correction is being developed to compute the strengths of the correctors $f_s = \lim_{t \rightarrow \infty} [f_1(t), \dots, f_M(t)]$ that minimize the deviation of the beam parameter r at a given constant perturbation:

$$r = \|\vec{x} - \vec{x}_0\| = \|\mathbf{R}\vec{f}_s\| < \varepsilon,$$

where \mathbf{R} is the response matrix; \vec{x} is the vector of the actual measured values; \vec{x}_0 is the target vector. The vector norm is defined as follows:

$$\|\vec{x}\| = \frac{1}{N} \sqrt{\sum_{i=1}^N x_i^2}.$$

It follows from (3.21) that the correction algorithm essentially consists in the inversion of the response matrix \mathbf{R} . However, in practice the matrix \mathbf{R} is often singular or almost singular, so one of the most widely used algorithms is the singular value decomposition (SVD). The response matrix can be written as $\mathbf{R} = \mathbf{U}\lambda\mathbf{V}^T$ and the inverse matrix, as $\mathbf{R}^{-1} = \mathbf{V}\lambda^{-1}\mathbf{U}^T$; where \mathbf{U} is the $m \times n$ full unitary matrix; λ is the diagonal matrix consisting of the eigenvalues of the matrix \mathbf{R} ; and \mathbf{V} is an orthogonal matrix, the columns of which are the eigenvectors of the matrix \mathbf{R} . To eliminate singularities at the calculation of \mathbf{R}^{-1} , the λ_k^{-1} values corresponding to small eigenvalues λ are set equal to zero. The number of the eigenvalues used to compute the inverse matrix \mathbf{R}^{-1} is chosen as a compromise between the accuracy and reliability of the correction algorithm: a larger number of eigenvalues provides a better convergence, but at the same time the correction process becomes more sensitive to the measurement errors and the noise of the electronics. In addition, the response matrix used for the correction can deviate from the real matrix of the magnet lattice, and therefore the correction process may consist of several consecutive iterations.

3.9.3 Computation of the transfer functions

Analysis of the time-domain processes occurring in the beam parameter stabilization system allows optimizing the system operation in real time. A typical scheme of a closed single-input-single-output (SISO) automatic control system is presented in Fig.3.44.

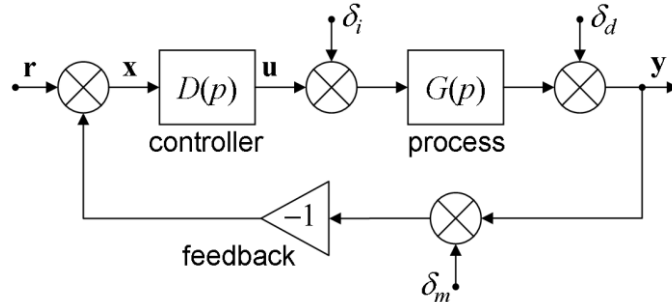


Fig. 3.44 First-order automatic control system

The controlled process and the control device (controller) are characterized by the frequency-dependent transfer functions $G(p)$ and $D(p)$, respectively, where p is the complex Laplace frequency. The stability of the system and its sensitivity to perturbations and noise are determined by the following functions:

$$\begin{aligned}
 T(p) &\equiv \frac{y}{r} = \frac{D(p)G(p)}{1 + D(p)G(p)} \\
 S_d(p) &\equiv \frac{y}{\delta_d} = \frac{1}{1 + D(p)G(p)} \\
 S_i(p) &\equiv \frac{y}{\delta_i} = \frac{G(p)}{1 + D(p)G(p)} \\
 S_u(p) &\equiv \frac{u}{\delta_d} = \frac{D(p)}{1 + D(p)G(p)}
 \end{aligned} \tag{3.22}$$

where $T(p)$ is the full (nominal) transfer function; $S_d(p)$ is the nominal sensitivity, which determines the perturbation suppression by the feedback; $S_i(p)$ is the sensitivity to input perturbations; $S_u(p)$ is the sensitivity of the control system. The state variables are also denoted in 3.44: \mathbf{r} is the target of correction; \mathbf{y} is the variable to control; \mathbf{x} is the error signal; \mathbf{u} is the correction action; δ_m is the measurement noise; δ_i and δ_d are the perturbations at the input and output of the process, respectively.

The classic computation of feedback is based on the study of zeros of the denominator in equations (3.22) using, for example, the Nyquist stability criterion in the following formulation: a closed-loop system is stable if the hodograph of the transfer function $D(p)G(p)$ of the open-loop system does not include the $(-1, 0i)$ point in the complex plane. If an open-loop system is unstable, for the closed-loop system stability it is necessary and sufficient that the hodograph of the transfer function $D(p)G(p)$ of the unstable open-loop system includes the point with the coordinates $(-1, 0i)$ $n/2$ times, where n is the number of the roots of the characteristic equation of the open-loop system with a positive real part. In this case a number of conditions must be observed, such as providing the necessary bandwidth, minimizing the mavericks during the regulation, providing a wide dynamic range of corrective actions as well as achieving maximum reliability in relation to the measurement errors and the model inaccuracies.

Typically, the feedback systems to stabilize the beam parameters in accelerators are developed and put into operation independently of one another, and the study of their interdependence and the reduction of parasitic relationships are often neglected. Nevertheless, for the systems to work stably and reliably it is necessary to take into account the possible cross-talk coupling between several parallel and possibly nested feedback loops at the design stage.

A typical cross-talk coupling is inherent, for example, to the systems for stabilization of the orbit and betatron tunes: although beam orbit stabilization at the micron level inhibits the

undesirable effects associated with the orbit deviation in the magnets and has a positive effect on the beam lifetime, it also imposes substantial limitations on other systems, in particular, those intended to stabilize the betatron tunes and the chromaticity, the measurement of which requires excitation of the beam jitter and, in case of chromaticity, even a change in the longitudinal momentum.

3.9.4 Orbit stabilization

Beam trajectory stability is essential for efficient operation of particle accelerators. Identification and minimization of noise sources at the accelerator design stage can significantly improve the situation. However, in many cases the required level of stability of the trajectory can only be achieved by using feedback systems. In particular, it is impossible to do without fast feedback in cases when the most severe conditions are imposed on the short-term (milliseconds - seconds) and medium-term (minutes - days) beam stability [54].

The main cause of beam trajectory distortion on the short-term and mid-term scales is usually a mechanical displacement of the magnets, especially quadrupoles, caused by vibrations of the soil, thermal effects, coolant motion, etc. Other sources of trajectory instability are oscillations of the supply current, which contain the harmonics of the mains frequency as well as stray electrical and magnetic fields.

In a typical feedback scheme intended to stabilize the beam trajectory, the input signals are supplied by a set of beam position pickups, and the corrective action is carried out using magnetic dipole correctors or electromagnetic kickers. The regulators are usually programmable signal processors of various types. In a local scheme, three or four magnetic correctors are used to create a local compensated effect stabilizing the position and angle of the electron beam at a desired point without affecting the rest of the orbit. A global feedback scheme which includes all the beam pickups and all the correcting dipole magnets is most often used to minimize the standard deviation of the orbit from a golden one, though other correction strategies are also possible.

The correction algorithm is usually based on the inversion of the response matrix, which relates the beam position at the locations of the pickups to the currents of the magnetic correctors. The inversion is executed by the method of expansion of the matrix in eigenvalues. This method allows us to represent a system of an arbitrary number of pickups and correctors interrelated via the response matrix in the transformed space, where each pickup is connected with one virtual corrector through a single coefficient. These coefficients correspond to the eigenvalues of the diagonal response matrix in the transformed space, which allows passing from the original MIMO system to a set of independent SISO feedback loops for each of the transformed channel of correction. The dynamics of each channel are determined by the low-frequency characteristic of the corrector, mainly by the eddy currents in the magnet yoke and the walls of the vacuum chamber. Another important parameter is the total delay time of the system, determined by the time of measurement and data processing and transmission. The typical delay time of modern feedback systems [55, 56, 57] is in the order of several hundreds of nanoseconds. Thus, each correction channel can be quite accurately described via a model consisting of a first-order low-pass filter and a delay line.

A proportional-integral-differential controller (PID controller) is most commonly used as a control element. With a feedback operating frequency of up to 10 kHz the optimal choice of the PID controller parameters allows effective stabilization of the beam orbit in the frequency band of 100-150 Hz. The bandwidth in local loops of a fast feedback system can be extended using correctors without magnetic cores, while a slower global feedback system usually includes all the available standard orbit correctors.

The stable components of the perturbation spectrum such as the mains frequency and its harmonics can be effectively suppressed with special narrowband feedback loops. Since filters tuned to different frequencies are decoupled, they can operate in parallel. Moreover, since the perturbations introduced by the harmonics of the mains frequency usually change very little in

time, they can be suppressed even if the perturbation frequency exceeds the frequency limit of a system with open feedback system.

In systems for fast orbit stabilization, data are processed using different computing platforms such as field-programmable gate arrays (FPGA), digital signal processors (DSP) and general-purpose computers with real-time operating system, which are integrated in the control system of accelerator complex. Ethernet with modified low-level drivers is often used in fast communication networks.

3.9.5 Fast feedback systems

At present, most accelerator facilities are equipped with fast feedback systems for the turn-by-turn suppression of the transverse and longitudinal instabilities of beam motion.

The development of digital technology allows creating bunch-by-bunch feedback systems, which control the motion of each bunch in the multi-bunch mode [58, 59, 60]. All digital feedback systems are similar to one another in their design. The flowchart of a multi-bunch feedback system is shown in Fig. 3.45. Electrostatic or stripline pickups, the signals of which are processed by analog hybrid circuits outputting signals proportional to the horizontal and vertical coordinates of the beam and its intensity, are used as the beam position sensors. These signals are then detected and digitized. The digital data are processed either by field-programmable gate arrays (FPGA) or by a digital signal processor (DSP), which calculates the strength of the pulse kicker, which impacts on the beam. Filters with finite impulse response, FIR-filters, are widely used for signal processing.

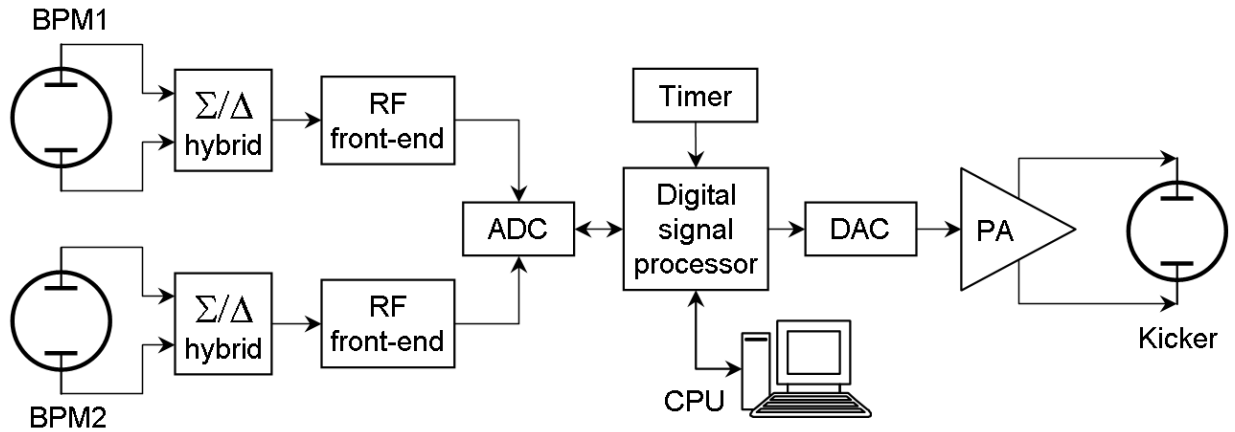


Fig. 3.45 Scheme of a digital feedback system.

It should be noted that the use of stripline pickups and kickers with the directivity allows simultaneous stabilization of the electron and positron bunches circulating in opposite directions, the same striplines used for both types of particles [61].

Using two pickups allows calculating the transverse beam position and momentum at each turn. In the linear approximation, the coordinate transformation by the section of magnet lattice between the pickups looks as follows:

$$x_2 = x_1 \sqrt{\beta_2 / \beta_1} (\cos \Delta\phi_{12} + \alpha_1 \sin \Delta\phi_{12}) + x'_1 \sqrt{\beta_2 \beta_1} \sin \Delta\phi_{12}, \quad (3.23)$$

where $x_{1,2}$, $x'_{1,2}$, $\beta_{1,2}$, $\alpha_{1,2}$ are the values of the position, momentum, and the lattice functions at the first and second pickup, respectively; ϕ_{12} is the betatron phase advance in this section. Conversion of (3.23) allows expressing the transverse momentum of the beam center of mass at the azimuth of the first pickup via the x_1 and x_2 positions measured by both the pickups. Applying a similar conversion, we obtain the beam position x_K and momentum x'_K in the kicker.

$$x_K = x_1 C_{1K} + \frac{x_2 - x_1 C_{12}}{S_{12}} \quad x'_K = \frac{1}{\beta_K} \left[-x_1 (\alpha_K C_{1K} + S_{1K}) - \frac{x_2 - x_1 C_{12}}{S_{12}} (C_{1K} - \alpha_K S_{1K}) \right], \quad (3.24)$$

Here

$$C_{1K} = \sqrt{\beta_K / \beta_1} \cos \Delta\phi_{1K}, \quad S_{1K} = \sqrt{\beta_K / \beta_1} \sin \Delta\phi_{1K}, \quad (3.25)$$

$$C_{12} = \sqrt{\beta_2 / \beta_1} \cos \Delta\phi_{12}, \quad S_{12} = \sin \Delta\phi_{12},$$

ϕ_{1K} is the betatron phase advance in the section between the first pickup and the kicker; β_K and α_K are the lattice functions at the azimuth of the kicker.

The kicker voltage is calculated as follows:

$$V_{\text{kick}} = \frac{E}{e} \frac{d}{L} \left(\text{Re} K_{\text{FB}} x'_K + \text{Im} K_{\text{FB}} \frac{x_K}{\beta_K} \right), \quad (3.26)$$

where $\text{Re}K_{\text{FB}}$ and $\text{Im}K_{\text{FB}}$ are the coefficients of the resistive and reactive feedback, respectively; E is the beam energy; L is the kicker length; d is the distance between the plates.

So, the signal processing should consist in the following operations:

- setting the feedback coefficients $\text{Re}K_{\text{FB}}$ and $\text{Im}K_{\text{FB}}$;
- measuring the beam position in the x_1 and x_2 pickups;
- calculation of the beam position and momentum in the kicker by formulae (3.24) and (3.25);
- calculation of the kick amplitude by formula (3.26).

Note that all the values in the formulae except x_1 and x_2 are computed beforehand, and the signal processor is used for fast computation of expressions of the $ax + by$ type. Fig.3.46 presents an example of computer simulation of the feedback in the Matlab-Simulink environment.

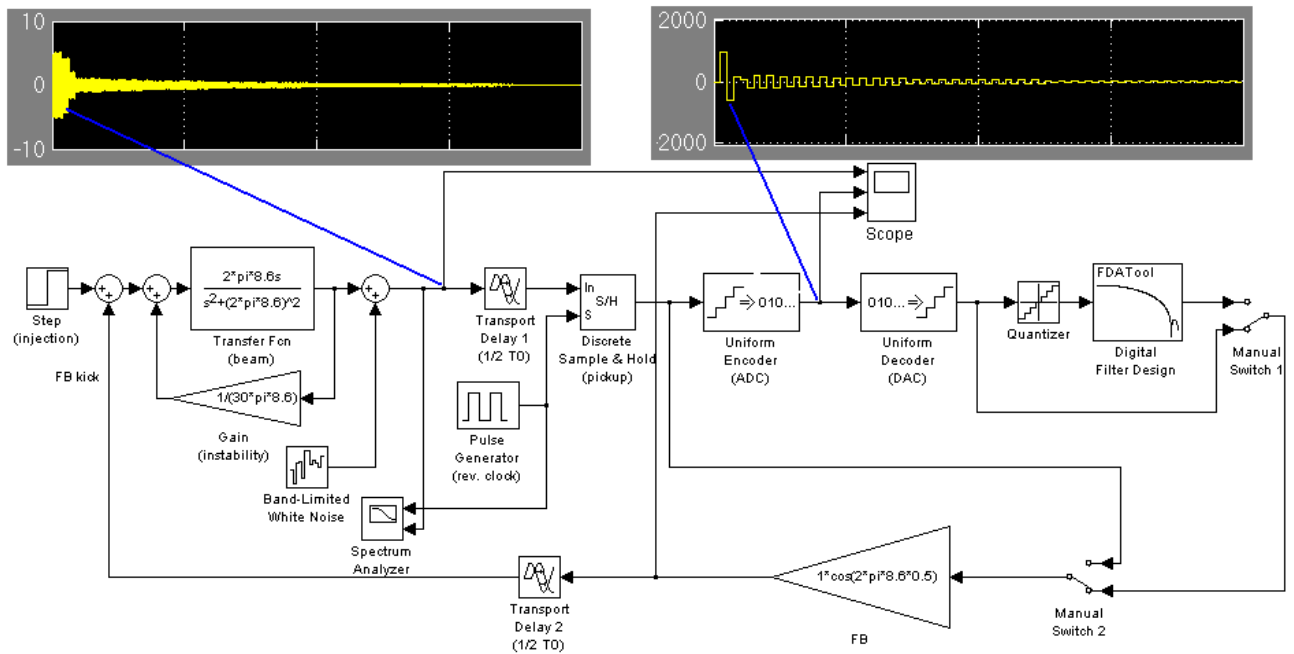


Fig. 3.46 Computer simulation of feedback system.

In the longitudinal feedback systems, the input signal is the deviation of the beam phase from the equilibrium one and broadband cavities are used as kickers [62, 63].

The technique of direct digitization of the RF signal of beam position pickups has developed recently [64]. Direct digitization allows transferring the signal to the low-frequency region and detecting the signal without complex analog electronics. This simplifies the system and reduces its cost as well as makes its setting more convenient.

Table 1. Parameters of KEKB, PEP-II and the C- τ -factory

	KEKB LER	KEKB HER	PEP-II LER	PEP-II HER	C-tau BINP
Energy, GeV	3.5	8.0	3.1	9.0	2.0
Circumference, m	3016.26	3016.26	2199.3	2199.3	766.6
Bunch, length, mm	4	4	11	11	10
Energy spread	$7.1 \cdot 10^{-4}$	$6.7 \cdot 10^{-4}$	$8.1 \cdot 10^{-4}$	$6.1 \cdot 10^{-4}$	$8.4 \cdot 10^{-4}$
Bunch-to-bunch distance, m	0.59	0.59	1.26	1.26	1.77
Horizontal emittance, nm	18	18	50		8
Vertical emittance, nm	0.36	0.36	2		0.04
Synchrotron frequency	0.01-0.02	0.01-0.02	0.03	0.05	$9.3 \cdot 10^{-3}$
Betatron tune (hor.)	45.52	47.52	36.57	24.57	47.54
Betatron tune (ver.)	45.08	43.08	34.64	23.64	30.57
Average beta function (hor.), m	10	10	10.84	14.5	15
Average beta function (ver.), m	10	10	9.95	13.84	15
Momentum compaction factor	$(1-2) \cdot 10^{-4}$	$(1-2) \cdot 10^{-4}$	$1.31 \cdot 10^{-3}$	$2.41 \cdot 10^{-3}$	$9.07 \cdot 10^{-3}$
Bending radius, m	16.3	104.5			8.25
Bending magnet length, m	0.915	5.86			0.454
RF voltage, MV	5-10	10-20	5.12	18.5	0.99
RF frequency, MHz	508.887	508.887	476	476	500
RF harmonic number	5120	5120	3492	3492	1300
Revolution frequency, kHz	99.4	99.4	136.3	136.3	391
Radiation damping time (long.), ms	43/23	23	40	37	15
Energy loss to SR, MeV/turn	0.81/1.5	3.5	0.87	3.57	0.343
Total radiation power, MW	2.1/4.0	3.8			0.586
Particles per bunch	$3.3 \cdot 10^{10}$	$1.4 \cdot 10^{10}$	$6 \cdot 10^{10}$	$2.7 \cdot 10^{10}$	$7 \cdot 10^{10}$
Bunch current, mA	0.52	0.22	1.3	0.59	4.4
Bunch peak current, A	158	67	104.5	47	134
Total beam current, A	2.6	1.1	2.1	1.0	1.71
Vacuum chamber	Cu ¹ Ø94 mm ² NEG inserts	Cu racetrack ³ 104×50mm ² Ø50mm NEG stripes	Straight sections: stainless steel Ø94mm arcs: Al ellipt. 95×59 mm ² +antechamber	1300 m: copper, 900 m: stainless steel	copper-plated aluminum 100×50 mm ²

¹ – low photodesorption coefficient, high thermal conductivity, possibility of shielding the X-rays.² – in order to avoid the resistive-wall multi-bunch instability.³ – in order to minimize the gap in the dipole magnets.

Table 2. Estimates for the instabilities at KEKB, PEP-II and the C-τ factory

	KEKB LER	KEKB HER	PEP-II LER	PEP-II HER	C-tau BINP
Microwave instability $I_{th} = \frac{\sqrt{2\pi}\sigma_{s0}}{R} \frac{\alpha}{Z/n} \frac{E}{e} \left(\frac{\sigma_E}{E} \right)^2$	$I_{th}=7.4 \cdot 10^{-6} B/(Z/n)$ $I_{th}=0.1 \text{ mA @}$ $Z/n=72 \cdot \text{mOhm}$ $I_b=0.52 \text{ mA}$	$I_{th}=1.5 \cdot 10^{-5} B/(Z/n)$ $I_{th}=0.2 \text{ mA @}$ $Z/n=76 \cdot \text{mOhm}$ $I_b=0.22 \text{ mA}$	$I_{th}=2.1 \cdot 10^{-4} B/(Z/n)$ $I_{th}=3 \text{ mA @}$ $Z/n=71 \cdot \text{mOhm}$ $I_b=1.3 \text{ mA}$	$I_{th}=2.2 \cdot 10^{-4} B/(Z/n)$ $I_{th}=9 \text{ mA @}$ $Z/n=76 \cdot \text{mOhm}$ $I_b=0.59 \text{ mA}$	$I_{th}=2.7 \cdot 10^{-4} B/(Z/n)$ $I_{th}=2.7 \text{ mA @}$ $Z/n=100 \cdot \text{m}\square$ $I_b=4.4 \text{ mA}$
Bunch lengthening	~20%	~20%			~50%
TMC instability $\frac{\Delta v}{\Delta I} = \frac{\sqrt{2\pi R} < Z_{\perp} \beta >}{\sigma_{s0} 8\pi E/e}$ $I_{th} = \frac{\sigma_{s0}}{\sqrt{2\pi R} < Z_{\perp} \beta > e} \frac{4\pi v_s}{E}$	$\Delta v_s/\Delta I_b=3.4 \text{ A}^{-1}$ (design) (0.38 - CDR) $I_{th}=1.5 \text{ mA @}$ $Z_T=99 \text{ kOhm}$ $\Delta v_s/\Delta I_b=4.2 \text{ A}^{-1}$ $\Delta v_s/\Delta I_b=1.5 \text{ A}^{-1}$ (measured.)	$\Delta v_s/\Delta I_b=0.44 \text{ A}^{-1}$ (design) $I_{th}=11.4 \text{ mA @}$ $Z_T=29 \text{ kOhm}$	$\Delta v_s/\Delta I_b=0.23 \text{ A}^{-1}$ (design) $I_{th}=32.6 \text{ mA @}$ $Z_T=22.5 \text{ kOhm}$	$\Delta v_s/\Delta I_b=0.1 \text{ A}^{-1}$ (design) $I_{th}=98.2 \text{ mA @}$ $Z_T=20 \text{ kOhm}$	$\Delta v_s/\Delta I_b=0.36 \text{ A}^{-1}$ (design) $I_{th}=13.1 \text{ mA @}$ $Z_T=39 \text{ kOhm}$
Longitudinal multi-bunch instability – HOMs of the RF cavities	60 ms	150 ms			
Transverse multi-bunch instability – RF HOMs of the RF cavities	30 ms	80 ms			
Transverse multi-bunch instability – resistive-wall CBI	~5 ms (suppressed by the feedback)		hor.: 1.41 ms ver.: 0.92 ms feedback damping time of 0.31 ms	hor.: 5.56 ms ver.: 3.85 ms	hor.: 170 ms ver.: 8.6 ms
Multi-bunch instability – ions		~1 ms (2D modeling) feedback is needed	Solenoids with a field of 30 G are used		
Multi-bunch instability – electron clouds	>0.4 ms Solenoids+feedback				

REFERENCES

1. A.N.Skrinsky Studies for a Tau-Charm Factory, SLAC-Report-451, October, 1994
2. C-Tau in Novosibirsk: Conceptual Design Report, BINP, Novosibirsk, 1995
3. E. Perelshtein et al. Proc. of the 3rd Workshop on the TC Factory, Marbella, Spain, 1-6 Jun 1993, 557-570
4. M.V. Danilov et al. Int. J. Mod. Phys. A, Proc. Suppl. 2A (1993) 455-457
5. E.Berger et al. ANL-HEP-TR-94-12, Feb 1994. 28pp
6. Yu.Aleksahin, A.Dubrovin, A.Zholents. In EPAC 90 Proc., vol. 1, 398-400
7. He-Sheng Chen. Nucl. Phys. Proc. Suppl. 59: 316-323, 1997
8. A. Faus-Golfe and J. Le Duff. NIM A372:6-18, 1996
9. J.Q. Wang, L. Ma, Q. Qin, C. Zhang. Status and performance of BEPC II, Proceedings of IPAC'10, Kyoto, Japan, 2010, WEXMH01, p. 2359.
10. P. Raimondi, Status of the SuperB Effort, presentation at the 2nd Workshop on Super B Factory, LNF-INFN, Frascati, March 2006
11. P. Raimondi and M. Zobov, DAΦNE Technical Note G-58, April 2003;
12. D. Shatilov and M. Zobov, ICFA Beam Dyn. Newslett. 37, 99 (2005)
13. M.Zobov (INFN LNF), for DAFNE Collaboration Team, DAFNE Operation Experience With Crab Waist Collision, arXiv:0810.2211v1
14. Ya.S.Derbenev, A.M.Kondratenko, A.N.Skrinsky. On the spin motion of particles in storage rings with arbitrary field. INP preprint, № 2-70 (1970).
15. Ya.S.Derbenev, A.M.Kondratenko, A.N.Skrinsky. Soviet Doklady (Physics) v. 192, № 6, pp. 1255-1258 (1970) (In Russian). Soviet Physics "Doklady", 15, pp 583-586 (1970) (translation)
16. N.Yu. Muchnoi, S. Nikitin, V. Zhilich. Proc. of EPAC 2006, Edinburg, Scotland
17. D.V.Pestrikov, NIM Phys. Res., Sect. A 336, 427 (1993)
18. K. Ohmi et al., Phys. Rev. ST Accel. Beams 7, 104401 (2004)
19. K. L. Brown and R. Servranckx, "First And Second Order Charged Particle Optics", AIP Conf. Proc. 127, 62 (1985).
20. J. Hagel, "Analytic Calculation Of The Off Momentum Closed Orbit In Storage Rings With Insertions And Sextupoles," CERN-LEP-TH-84-18.

21. P.Raimondi, D.Shatilov, M.Zobov, “Beam-Beam Issues for Colliding Schemes with Large Piwinski Angle and Crabbed Waist”, LNF-07-003-IR, Feb. 2007, e-Print: physics/0702033.
22. P.Raimondi, D.Shatilov, M.Zobov, “Suppression of beam-beam resonances in Crab Waist collisions”, Proc. of EPAC08, Genoa, Italy, 23-27 Jun. 2008.
23. M.Zobov et al., “Test of crab-waist collisions at DAFNE Phi factory”, Phys.Rev.Lett.104:174801,2010.
24. M.Zobov, “Beam-Beam Interaction in Novel, Very High Luminosity Parameter Regimes”, Proc. of IPAC10, Kyoto, Japan, 23-28 May 2010.
25. M.Bona et al., “A High-Luminosity Asymmetric e+e- Super Flavor Factory. Conceptual Design Report”, SLAC-R-856, INFN-AE-07-02, LAL-07-15, May 18, 2007, e-Print: arXiv:0709.0451.
26. D.Shatilov, E.Levichev, E.Simonov, “Application of Frequency Map Analysis to Beam-Beam Effects Study in Crab Waist Collision Scheme”, arXiv:1002.3733.
27. Ya.S.Derbenev et al. “Radiative Polarization: Obtaining, Control, Using”, Part.Acc. 8, 115, 1978.
28. I.A.Koop, A.V.Otboev, P.Yu.Shatunov, Yu.M.Shatunov.”Orbit and Spin transparent Siberian Snake and Spin Rotator with Solenoids”, SPIN2006, Nagoya, Japan, 2006.
29. A.A.Zholents and V.N.Litvinenko, “On the Compensation of Solenoid Field Effects by Quadrupole Lenses”, DESY-L-TRANS-289, Mar 1984. 9pp. Translation of Novosibirsk preprint IYF-81-80 (translation).
30. Ya.S.Derbenev, A.M.Kondratenko, “Polarization kinematics of particles in storage rings”, Sov.Phys.JETP 37:968-973,1973, Zh.Eksp.Teor.Fiz.64:1918-1929,1973.
31. V.I. Ptitsyn , Ph.D. Thesis, Novosibirsk, BINP, 1997 (in Russian).
32. V.I. Ptitsyn, (Brookhaven), Yu.M. Shatunov, (Novosibirsk, BINP), S.R. Mane, (Convergent Computing, Shoreham, NY). “Spin response formalism in circular accelerators”. Published in Nucl.Instrum.Meth.A608:225-233,2009.
33. V.N.Bayer et al., Yadernaya Fizika 36 (1982), 163. (in Russian)
34. G.K.Kotkin et al., Yadernaya Fizika 42 (1985), 925. (in Russian)
35. J. Le Duff, Proc. CERN Accelerator School, 2nd Advanced Accel. Physics Course, Berlin, 114 (1987).
36. H.Bruck, “Circular particle accelerators”, LA-TR-72-10, Los Alamos, NM, p.323.

37. A. Piwinski, in Handbook of Accelerator Physics and Engineering, edited by A. Chao and M. Tigner (World Scientific, Singapore, 1999), p. 125; K.Kubo, S.Mtingwa and A.Wolski, Phys. Rev. ST Accel. Beams 8, 081001 (2005).
38. Chao A. Physics of Collective Beam Instabilities. New York: Wiley, 1993.
39. Zotter B.W., Kheifets S.A. Impedances and Wakes in High-Energy Particle Accelerators. Singapore: World Scientific, 1998.
40. Dikansky N.S., Pestrikov D.V. Physics of intensive beams in storage rings. Novosibirsk: Science, 1989. (in Russian)
41. Zotter B., "Potential-Well Bunch Lengthening", CERN SPS/81-14 (DI), 1981.
42. Clarke J.A., Bunch Lengthening Thresholds on the Daresbury SRS, CCL Daresbury Laboratory, 1995.
43. Chao A.W., Tigner M., Handbook of Accelerator physics and Engineering, World Scientific, 2006.
44. Sacherer F. IEEE Trans. Nucl. Sci, NS-24 (1977) p. 1393.
45. Keil E., Schnell W. // CERN ISR-TH-RF 69/48 (1969).
46. Boussard D., CERN-Lab II/RF/75-2, 1975.
47. Boussard D. Observation of Microwave Longitudinal Instabilities in the SPS // CERN II/RF/Int.75-2 (1975).
48. Wiedemann H. Particle Accelerator Physics II, Springer-Verlag, 1995.
49. Fabris A., Pasotti C., Svandrlík M., Coupled Bunch Instability Calculations for the ANKA Storage Ring, Proc. of EPAC-98, Stockholm, Sweden, 1998.
50. Dobbing G.S., Wolski A., Instability Threshold Calculations for DIAMOND, Proc. of EPAC-2000, Vienna, Austria, 2000.
51. Ohmi K. Beam Instabilities // International Symposium "Forty Years of Lepton Colliders" (COLLID04) Novosibirsk, Russia, 2004.
52. Steinhagen R.J. Real Time Feedback on Beam Parameters // Proc. of APAC 2007. Indore, India, 2007.
53. Boege M. Achieving Sub-micron Stability in Light Sources // Proc. of EPAC 2004. Lucerne, Switzerland, 2004.
54. Bulfone D. Overview of Fast Beam Position Feedback Systems // Proc. of EPAC 2008. Genoa, Italy, 2008.
55. Masuzawa M., Flanagan J.W., Funakoshi Y., Oide K. IP Orbital Feedback for Collision Tuning at KEKB // Proc. of EPAC 2000. Vienna, Austria, 2000.
56. Hendrickson L., Gromme T., Grossberg P. et al. Slow Feedback Systems for PEP-II // Proc. of EPAC 2000. Vienna, Austria, 2000.

57. Abbott M.G. Performance and Future Developments of the Diamond Fast Orbit Feedback System // Proc. of EPAC 2008. Genoa, Italy, 2008.
58. Tobiyama M., Kikutani E., Flanagan J. W., Hiramatsu S. Bunch by Bunch Feedback Systems for the KEKB Ring // Proc. of PAC 2001. Chicago, USA, 2001.
59. Weber J., Chin M., Doolittle L. PEP-II Transverse Feedback Electronics Upgrade // Proc. of PAC 2005. Knoxville, USA, 2005.
60. Yao C.-Y., Norum E., Di Monte N. An FPGA-Based Bunch-to-Bunch Feedback System at the Advanced Photon Source // Proc. of PAC 2007. Albuquerque, USA, 2007.
61. Cherepanov V., Dementev E., Levichev E. et al. Transverse Bunch-by-bunch Feedback for the VEPP-4M Electron-positron Collider // Proc. of DIPAC-2007. Venice, Italy, 2007.
62. Arbuzov V.S., Gorniker E.I., Kenjebulatov E.K. et al. Feedback System for Damping of Longitudinal Bunch Oscillations in VEPP-4M Collider // Proc. of RuPAC 2006. Novosibirsk, Russia, 2006.
63. Yujong Kim, Busch W., Wang M. et al. New Generation Digital Longitudinal Feedback System for Duke FEL and HIGS Facilities // Proc. of PAC 2007. Albuquerque, USA, 2007.
64. Nakamura T., Kobayashi K., Zhou Z. Bunch by Bunch Feedback by RF Direct Sampling // Proc. of EPAC 2008. Genoa, Italy, 2008.